공학박사 학위논문

The Electrochemical Properties of Porous Carbon for the Li-ion and Li-Sulfur Batteries

리튬-이온 및 리튬-황 전지에서의 다공성 탄소물질의 전기화학적 특성

2016 년 2 월

서울대학교 대학원

공과대학 화학생물공학부

김 정 준

Abstract

The Electrochemical Properties of Porous Carbon for the Li-ion and Li-Sulfur Batteries

Jung-Joon Kim

School of Chemical & Biological Engineering

Seoul National University

The role of the energy storage in the society is becoming increasingly important. Until recently, the applications of energy storages have been generally limited to portable devices, and the energy storage companies have been unable to fully tap into the markets with great potential, such as electric vehicles and storages for residences. The market conditions, which favor the economically more viable fossil fuel, have been a formidable obstacle. However, today, the society seeks cleaner energy, which could replace the conventional fossil fuel, in order to provide a more sustaining environment for the next generations. Various factors have contributed to the change. For instance, the societies are alerted by the abnormal weather conditions such as El Niño and dust bowl that wreak

havoc to cities and cause much dismay to its inhabitants. Moreover, the monopoly of oil producing countries that causes lopsided energy dependence for the industrialized countries have created a general consensus that energy independence is not an option, but a priority. The recent scandal involving Volkswagen and their complicit in the manipulation of the public regarding the mileage and emission of their diesel cars has further fueled the society's interest in the electric vehicles.

While such attentions are highly encouraging for the engineers, scientists, and corporations involved in the energy storage sector, the means to provide suitable energy storages for the needs of the society is yet to be realized. In the case of lithium-ion battery (LIB), which is already commercialized by several companies in the world, there is still much room for advancement regarding its specific capacity and the rate capability in order to meet the requirements of energy intensive applications such as electric vehicles and storages for residences. This is not to say that there has been lack of effort in attempts to improve the aforementioned limitations. On the contrary, the energy storage is one of the most popular research topics in the academia and numerous papers are published every year. The real challenge, I believe, is maintaining the effort to truly understand science of the electrochemical system using both novel and conventional techniques, despite the unrealistic standards set by institutions and governments that favor reports of new materials with astounding cyclability and rate performance in high impact factor journals. Such limitations have encouraged the researchers to seek for quick

reports on novel design of materials and their performance, which deserves some merit, but they often lack the depth for further advancement. Often, a publication means the end to the research regarding that material for many engineers and scientist. In this regards, I believe I have tried to evade such tendencies and made an effort to truly understand the electrochemical phenomena occurring within the porous carbon structures.

The first chapter of the thesis introduces the general overview of the Li-ion and Li-S batteries. The part includes the discussion of the critical issues that are under investigation in academia regarding each electrochemical system. Furthermore, a part explaining the overall objective of the dissertation is included.

The second chapter of the thesis discusses about the activation of micropore-confined sulfur within hierarchical porous carbon for lithium-sulfur batteries. Hierarchical porous carbon is often used in Li-S batteries due to the widely perceived benefits regarding the wide range of pore sizes. However, such notions are based solely on demonstrations of improved cyclic performances, and specific evidence to prove the utilization of the pores is yet to be found. Herein, we report, for the first time, the evidence for gradual activation of micropore-confined sulfur within porous carbon structures. By systematic comparison of microporous and hierarchical porous structures, we show that at sufficiently low current, sulfur infused hierarchical porous structures display a slowly activated and reversible reaction at 1.75 V vs Li/Li+ during discharge. This is in addition to the conventionally reported two voltage plateau at 2.3

and 2.1 V. Furthermore, the effects of LiNO3 decomposition on the system and the electrochemical mechanism behind the activation process is elucidated. Overall, the findings supplement the currently known electrochemical mechanisms occurring within porous structures and pave the way for more efficient utilization of hierarchical porous structures for applications in Li-S batteries.

The third chapter of the thesis discusses about the improved electrochemical performance of a three-dimensionally ordered mesoporous carbon based lithium-ion battery using vinylene carbonate as an electrolyte additive. Within this study, the effects of vinylene carbonate (VC) as an electrolyte additive on a 3-dimensionally ordered mesoporous carbon (3DOmC) based lithium ion battery (LIB) are investigated. Our investigation reveals an optimal concentration of VC, which improves the discharge specific capacity at the 100th cycle to 844.3 from 684.3 mAh g-1, and improves the first cycle's Coulombic efficiency to 32.4 from 23.7%. The improvements are revealed to be a result of the reduced charge transfer and solid electrolyte interface (SEI) resistance, enabling better permeability of Li ions. This work demonstrates that VC is a viable electrolyte additive in improving the performance of a non-graphitic carbonaceous material.

The studies mentioned above addresses the most critical issues in each system and provides a stepping stone for further research to establish ideal solutions. We hope to see the fruition of hard work in the near future.

Keywords: Electrochemistry, Surface analysis, Lithium-ion battery, Lithium-sulfur battery, Porous carbon

Student Number: 2012-31299

Contents

List of Tables

List of Figures

Chapter 1. Introduction

1.1. Background on energy storages

1.1.1. The science behind the device

The term battery refers to an energy storage device that stores energy in the form of chemical energy in its electrodes. A cell consists of two electrodes, one of which is the negative electrode (commonly but a misguided term is an anode) and the other is the positive electrode (commonly but a misguided term is a cathode). Through oxidation (loss of electron from the electrode) or reduction (gain of electron to the electrode) of its electrodes, the chemical energy is converted to the electrical energy, which could be used to power various electronic devices. The chemical energy can be quantified in Gibbs free energy, G, whereas the electrical energy is related to it's the cell potential, E. The two parameters have the following relation between them:

$$\Delta \mathrm{G} = \mathrm{G}_{anode} - G_{cathode} = -nFE \ (eq. 1)$$

where n refers to the number of electrons involved during the reduction or oxidation of the electrode, F is the faraday constant, and E is the cell potential. As can be seen from the eq. 1, the anode and cathode have different chemical energy. Due to the difference of the chemical energy between the cathode and anode, battery is able to supply energy spontaneously when connected to electronic devices. The energy is finite and as the

power is supplied the chemical energy is drained out of the battery, which reduces the Gibbs free energy difference between the cathode and anode. During this process, commonly termed discharge, lithium ions and electrons from the negative electrode are transferred to the positive electrode through external circuit and electrolyte, accordingly. Hence, oxidation occurs in the negative electrode and reduction occurs in the cathode. As mentioned before, the transfer of electrons and lithium ions from the negative electrode to the positive electrode occurs spontaneously, as it is natural for water to flow from top to bottom. The reverse process, on the other hand can only occur if external energy is supplied to the system. For instance, in order to transport water from the bottom to the top, an additional energy is required, e.g., adenosine triphosphate is required for a person to carry a bucket of water to the top or electricity required or electricity is required for the pump to transport the water to the top. Therefore, in the case of rechargeable batteries, we connect the batteries to the charger, which supplies external energy to the system. Within the system, a reverse process of discharge, termed charge, occurs. In this case, lithium ions and electrons from the positive electrode are transferred to the negative electrode through external circuit and electrolyte.

Although chemical energy is a convenient term to describe the state of a compound, another term often used is the chemical potential. Chemical potential is a form of potential energy that can be absorbed or released during a chemical reaction and has the following relation with the Gibbs free energy:

$$\mu_i^{\alpha} = \left(\frac{\partial G}{\partial n_i}\right)_{T,P,n_j} (eq.2)$$

Where μ is the chemical potential, G is the Gibbs free energy, n_i is the number of particles of species i, T is the temperature, and P is the pressure. As can be see, when the temperature, pressure, and species j remain constant, the chemical potential is the slope of the free energy with respect to the number of particles of the species i. In other words, the chemical potential is dependent on the change in Gibbs free energy when the number of species i change. It has been mentioned that the chemical potential has a relation with the cell potential as shown in eq. 1 Therefore, the cell potential, represented in units of Volt, can be thought of as the concentration of chemical species within the system that stores the Gibbs free energy. In the case of electrochemical systems that uses lithium ions, we can think of the change in Voltage as the change in the concentration of lithium ions. For a system at equilibrium, Nernst equation can describe the relation between the concentration of oxidation/reduction species and the cell potential:

$$v_A\, A + ne = v_c C$$

$$\mathrm{E}_{eq} = \mathrm{E}^0 + \frac{RT}{nF} \ln \frac{a_A^{V_A}}{a_C^{V_C}} (eq.3)$$

where a refers to the activity, which is closely related to the concentration of the chemical species. From the eq.3 mentioned above, one can deduce that chemical species within the electrode store energy and using the energy or resupplying the energy involves changing of its concentration.

1.1.2. Lithium ion battery

LIB consists of a cathode, an anode, electrolyte, and a separator as illustrated in Fig. 1.1. The cathode and anode are separated by a separator and electrolyte. Common electrolyte used is an organic electrolyte, which transports lithium ions between the anode and cathode. Generally, cyclic carbonate and linear carbonate are mixed together to have optimal dielectric constant (ε) and viscosity. Linear carbonate, such as diethyl carbonate (DEC), has low dielectric constant and low viscosity than those of cyclic carbonate. Low viscosity allows the lithium ions to move easily within the solvent whereas low dielectric constant inhibits facile dissociation with the salt due to the large attractive interaction between the cation and anion. The relationship between the dielectric constant and the electrostatic force is as follows:

$$\mathrm{F} = \frac{1}{4\pi\varepsilon_0\varepsilon}\frac{qQ}{r^2} (eq.4)$$

where F is the electrostatic force, q and Q are two point charge, ε_0 is the dielectric constant in vacuum, and r is the distance between two charges. As one can see, as ε decreases, the electrostatic force between the two charges increase, making it hard to dissociate. As a mitigation, cyclic carbonate such as ethylene carbonate (EC) is added into the electrolyte. In contrast to DEC, EC has high viscosity and high dielectric constant. Hence, the mixture of solvents provides an optimal viscosity and dielectric constant suitable for the LIB.

Separator acts as a physical barrier between the cathode and anode materials to prevent short circuit. The electrical separation between the cathode and anode material is critical, since it would cause self-discharge otherwise. Moreover, the separator is critical to the safety of the energy storage. Inadequate separation causes concentration of current to a particular region, which accumulates heat and leads to a run-away reaction. Separators that are used commercially are mixtures of polyethylene (PE) and polypropylene (PP), derivatives from crude oil. Although, the separator's role as a barrier between the cathode and anode was emphasized, an equally important role is the medium for the lithium ion transfer. Microscopic pores are developed within the polymeric membrane, which allows the solvents and lithium ions to move easily.

Generally, cathode materials possess lithium intercalation potential above 3 V vs Li/Li^+. Such potential is necessary for an adequate potential difference between the anode and cathode material. An ideal positive electrode material operates at high potential with a minimal structural and volumetric change. The molecular mass must be small to reduce the specific capacity. Moreover, the structure must allow rapid diffusion of lithium ions. Reported cathode materials material can be classified into three types (Fig. 1.2).

The first type is a layered structure, which is one of the most commonly used materials. A well-known example is $LiCoO_2$, which is developed by Prof. Goodenough. The material operates at a high potential and a wide temperature range. It also allows fast lithium ion diffusion through its two dimensional lithium ion pathways, and has good life

span depending on the set potential range. The downside is its structural instability beyond 4.2 V vs. Li/Li^+, and the high cost and toxicity of cobalt. Moreover, the specific capacity is limited to 130 mAh g^{-1} [1]. $LiNiO_2$ was also developed as an alternative to $LiCoO_2$. Although it can store more Li ions and is generally cheaper than $LiCoO_2$, the studies, however, suggest that Ni ions replace Li in the Li layer due to the similarity in size, causing cation mixing. The cation mixing impedes Li ion diffusion and prevents the synthesis of desired composition unless the experiment is performed at high O_2 pressure. As a result, solid solution of $LiNiO_2$ and $LiCoO_2$ was suggested, which has energy density about 150 mAh g^{-1}. However, in this case, the discharge potential is lower than that of $LiCoO_2$.

The second type of cathode has a spinel structure. $LiMn_2O_4$ is a primary example of a spinel structure. Its specific capacity is about 100-120 mAh g^{-1}. While the specific capacity of $LiMn_2O_4$ is lower than that of $LiCoO_2$, its three dimensional lithium ion pathway makes it very appealing in terms of the rate capability. Other advantages include simple synthesis procedures, fair stability, and economic viability. The downside of the material is that during the reaction an asymmetric lattice expansion and a contraction of the electrode from the Jahn-Teller distortion of Mn^{3+} ion occur at 3.7 V [2]. As a result, the dissolution of Mn^{3+} degrades the cell performance.

The third type of cathode has an olivine structure. A widely known olivine structure is $LiFePO_4$, which has a one dimensional Li ion pathway. Although, it only has one dimensional Li ion pathway, its reaction voltage (3.54 V) lies within a potential range at

which the electrolyte decomposition is minimal. Moreover, Fe is present in abundance and is eco-friendly, which caused it to become very appealing to the energy storage community. Its specific capacity is ~170 mAh g^{-1}, but the material also possess some downsides, which include poor electron and ion conductivity.

In the case of the anode materials, they are generally materials with low chemical potentials (Fig. 1.3). An ideal anode material should have a potential a little above that of Li metal in order to maximize the cell potential but mitigate the plating of Li metals. Moreover, the material should have high volumetric and gravimetric energy density along with a fair rate characteristic, good cyclability, and safety. Graphite is the most widely used and commercialized anode material due to its negative redox potential (0.1-0.2 V vs. Li/Li^+) and structural stability. The insertion of Li ion into carbon occurs as shown below:

$$Li_xC \leftrightarrow xLi^+ + xe^- + C$$

Depending on the type of carbon used, x is varied. Broadly speaking, carbon can be classified into two types, graphitic and non-graphitic. The graphitic carbon has layered structures with various degree of structural defects, e.g., natural graphite, artificial graphite, and pyrolytic graphite. In contrast, the non-graphitic carbon contain many defects, and its structure does not have a long-range crystallographic order in the c-direction. A highly crystalline graphite can take one Li per six carbon atoms, which equates to specific capacity of 372 mAh g^{-1} [3]. On the other hand, non-graphitic carbon with high surface

area has electronically and geometrically non-equivalent sites, resulting in much higher specific capacity. However, the material also displays much higher irreversible capacity.

Alternatives to carbonaceous material has been extensively investigated. Among them, metals such as Sn, Sb, Si, Ge, Al, and G have been suggested. The metals alloy with Li over 0 V Li/Li^+ and show much higher specific capacity than that of graphite. A common problem among such materials is the severe volume expansion/contraction during charge/discharge. The repeated change in volume leads to cracks within the structures of active material, resulting in electrical disconnection [4].

Other alternative anode materials include the transition metal oxides. For such materials, two types of reaction mechanisms are widely reported to occur. First is the insertion mechanism, and next is the conversion reaction as shown below:

$$MO_x + yLi^+ \leftrightarrow M_yLiO_x \text{ (Insertion reaction)}$$

$$MO_x + 2xLi^+ \leftrightarrow M + 2xLi_2O \text{ (Conversion reaction)}$$

During the insertion reaction, Li^+ ions intercalate into the metal oxide host while the M-O bonds remain unbroken. The conversion reaction occurs next, producing a large reversible capacity of 600-1000 mAh g^{-1}. During the charge, a nanostructure of M/Li_2O enables reoxidation of M. The conversion reaction is also reported to occur in phosphides and fluorides [5]. The material, however, exhibits large overpotential and hysteresis [6].

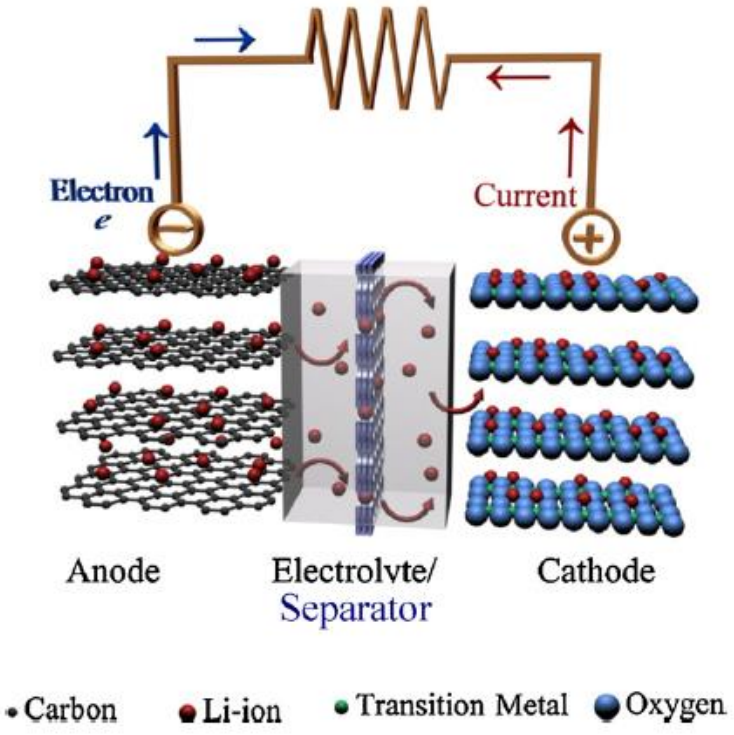

Figure 1.1. Schematic of LIB consisting of cathode, anode, electrolyte, and separator [7].

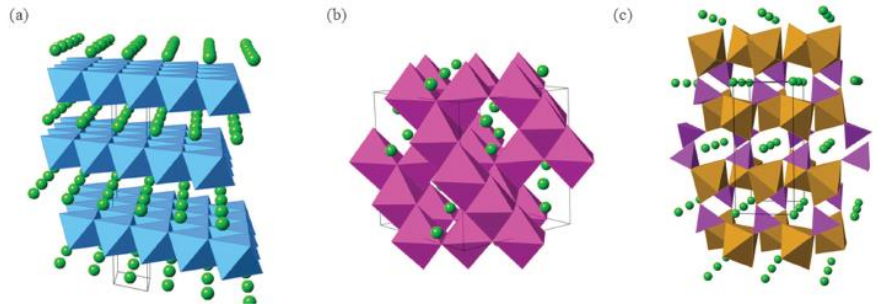

Figure 1.2. Three types of cathode materials. a) Layered b) Spinel c) Olivine [8].

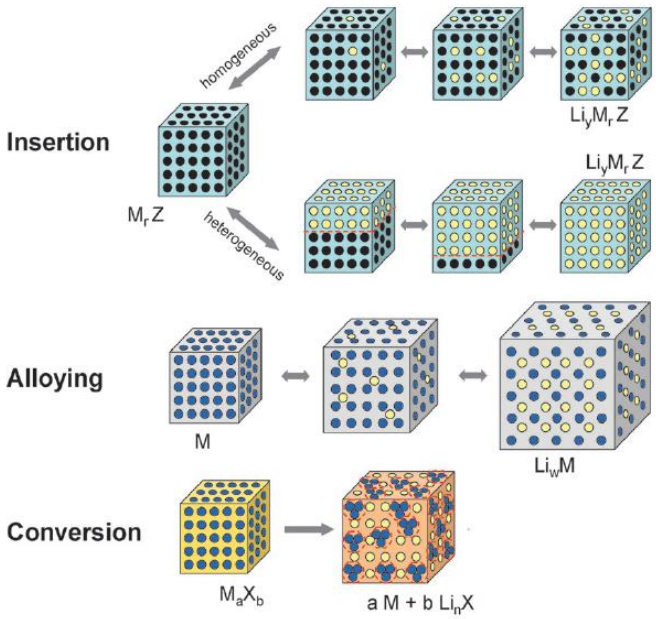

Figure 1.3. Schematic of different reactions for the anode material [9].

1.1.3. Lithium sulfur battery (Li-S battery)

Li-S battery has a high potential to be largely successful in the emerging energy storage market, such as those of electric vehicles and storages for residences. Li-S battery offers a high theoretical capacity of 1675 mAh g^{-1}. Furthermore, a large amount of sulfur is produced as a left from the refineries. Sour oil produces from parts of the world contains high contents of sulfur, which is unsuitable component as a fuel. Hence, large stocks of Sulfur separated from petroleum is left and continues to be accumulated. The high capacity is derived from conversion of sulfur to lithium sulfide (Li_2S), which is equivalent to accepting two electrons per sulfur atom. This is higher than those of high capacity transition metal oxides, which accepts either one or less than one per transition metal oxides [10]. Unfortunately, Li-S batteries have critical problems, like many other energy storage systems that are under research that much be resolved before being suitable for commercialization.

First of all, the conversion reaction results in a huge volumetric change of approximately 80%, which could contribute to a structural instability. Moreover, the sulfur and lithium sulfide produced from the reaction with lithium are both insulators. Hence, often a large amount of sulfur is used as a conductive agent for the electrode, which reduces both the specific capacity and the volumetric capacity of the electrode. Another critical problem is the dissolution of polysulfide, an intermediate that is produced during the conversion of sulfur to lithium sulfide. The dissolution of the active material into the electrolyte causes a major problem for the system, since it results in the loss of

active material and self-discharge upon contact with the counter electrode. Since polysulfide is a mobile chemical specie, without a proper barrier, it could cause a havoc within the system by diffusing into places where it is not required. Lastly, the utilization of sulfur requires a Lithium source within the system. The most commonly used source is lithium metal, which is widely known for dendrite formation. Such issues have to resolved altogether before Li-S battery can be suitable for commercialization.

Similar to LIB, Li-S battery consists of a cathode, an anode, and organic electrolyte. A schematic of the cell is shown in Fig. 1.4. The cathode usually consists of sulfur, conducting agent, and binding agent, whereas the anode is the lithium metal. For the electrolyte, usually ether-based electrolyte is employed. In order for the cell to operate, the reaction of sulfur with lithium ion is required. Therefore, oxidation occurs on the lithium anode, producing lithium ions and electron from the negative electrode. The lithium ion is migrated to the cathode through electrolyte, whereas the electrons are transferred to the cathode through external circuit. At the cathode, reduction occurs, where the sulfur reacts with lithium ions and accepts electron from the external circuit. At room temperature, the most stable allotrope of sulfur atoms is the octasulfur or cyclo-S_8, a homocyclic ring of sulfur. During the reduction, sulfur is first reduced to long-chain polysulfides. Most researchers agree that this reduction occurs during the first voltage plateau shown at ~2.3 V. Polysulfides are mobile chemical species, which are known to dissolve into ether-based electrolyte. The change in the color of electrolyte is

often observed when discharge below 2.3 V, which results from the dissolution of polysulfide. Upon further reduction to 2.1 V, another voltage plateau appears, which most researchers agree is where the formation of Li_2S start to occur. Since the thermodynamic cell potential of conversion of sulfur to Li_2S is 2.15 V, the general consensus is deemed correct. An interesting point is that most papers published on Li-S battery report voltage profiles with the range between 1.5 and 3 V with the current rate of 1 C (1675 mA g^{-1}). A schematic of the general voltage profile shown for a Li-S is shown in Fig. 1.5.

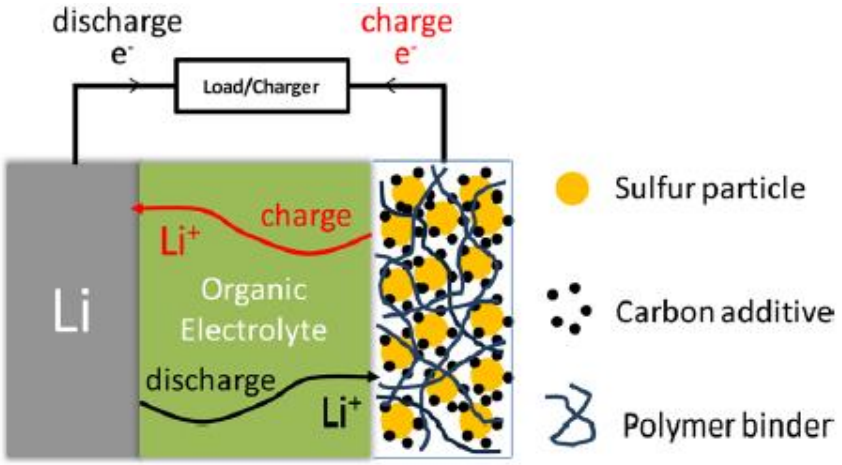

Figure 1.4. Schematic of Li-S battery during charge and discharge [10].

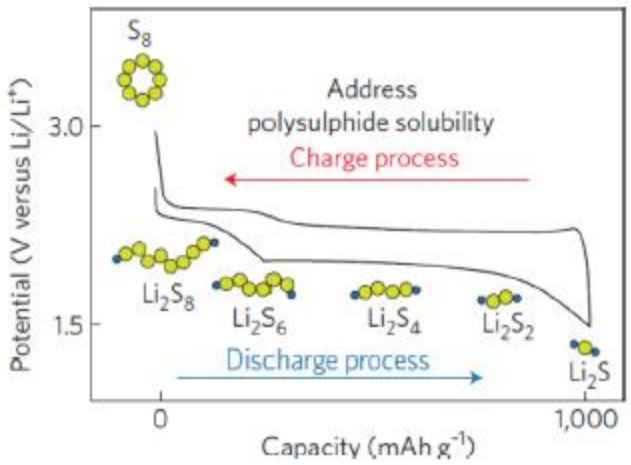

Figure 1.5. Voltage profile of a Li-S cell [11].

1.2. Recent progress in energy storage systems.

1.2.1. Research trends in LIB

Since the introduction of a lithium metal based battery in the late 70's (TiS_2/Li cell by Whittingham), much progress has been made. Today, LIB is used in most of the mobile devices and active research is on-going for further application into electric vehicles and storages for residences. The research trend that will be discussed in this section is based on papers published on various papers. Therefore, it will show the directions that the researchers in Academia are following which may or may not be suitable for commercial applications.

The major trend in the academia for many years has been nano sizing and developing structures that allow better diffusion of electrolytes. The attempt is logical since the ultimate goal is to improve the energy density of the material that will enable longer battery time with the same mass/volume of active material. For any applications, it is best for the energy storages to take the least amount of space and/or mass available. Therefore, nano sizing was deemed suitable for maximizing the energy density, since it provides the more surface area for a given amount of material. Increased surface area creates more reactive sites for Li ions, leading to an increased capacity. Furthermore, researches have been done to achieve efficient designs of the active materials. For a facile lithium ion diffusion, it is important to realize what the rate determining step is within the material. In the case of LIB, researchers generally agree that the energy

required to desolvate Li ions or the solid-state diffusion of Li ions diffusion is the rate determining step. The methods to reduce activation energy required for desolvation are limited due to the restrictive selection of suitable salts and solvents. On the other hand, the reduction of solid-state diffusion path is more manageable, since it requires nanosizing of the active material, reducing the length of solid state diffusion path for the Li ions. Moreover, researchers have tried to facilitate electrolyte diffusion within the active material by creating ordered or disordered porous structures. Such designs allow facile diffusion of electrolyte into the structure, and it was expected that the designs would assist against depletion of li ions on the surface of active material. A paper by Peter G. Bruce, Bruno Scrosati, and Jean-Marie Tarascon summarizes the effort very well [12].

The efforts mentioned above are very creative and displays the art of synthesis at utmost level. While such ideas are very well intended and possess inherent academic values, the applicability of the materials for commercial applications is still under question. Nanostructuring and nanosizing lead to the increase of surface area, which increases the sites for Li ion to diffuse in and react, but at the same time, it creates more decomposition products on the surface of the active material. Most of the cathodes and anodes operate at potential ranges, where electrolyte is unstable. Due to the decomposition of electrolyte on the surface of the active material, solid electrolyte interface (SEI) is produced. In the case of nanostructures, thicker SEI is produced due to the large surface area. SEI is known to be electronically insulating, but allows Li ion diffusion.

Therefore, a minimal amount of SEI is required to prevent further decomposition of electrolyte and allow Li ions to diffuse in and react with the active material. However, if the production of SEI is not minimized, the irreversible capacity and the corresponding amount of lithium ion lost to the production of SEI could become significant. Although such problems are not clearly visible in the experiments done in the papers, which often uses Lithium metal as an anode, in commercial applications, which use an electrode with limited amount of Li ion source, a high irreversible capacity could prove to be devastating. Unfortunately, the publications on nanostructuring of the active material are written to emphasize the merits of its structure design and often ignore problems regarding the irreversible capacity. Fortunately, researchers who major in electrochemistry and related areas are very well aware of such problems and are working to advance the interface between the electrolyte and electrode. A part of the study within this thesis discusses the method to enhance the chemical property of SEI in order to improve the discharge capacity of a porous carbon with high surface area.

1.2.2. Research trends in Li-S battery

As mentioned in the section 1.1.2, the primary problems of Li-S cell can be summarized as follows.

- Low electronic and ionic conductivity.
- Dissolution of polysulfide.
- Volume expansion around 80%
- Lithium metal; reactive and dendrite formation.

For some of the problems, extensive researches are done until now, while for others due to the considerable experimental difficulty the extent of investigation has been limited until now. It is interesting to note that the first of the three problems are related to the active material itself. Sulfur itself is not a very attractive material considering such properties. However, sulfur has a considerable cost merit which simply cannot be passed upon, hence there has been extensive research on the subject. Although, there are still many obstacles left for commercialization, the solutions provided by the researchers have the potential to resolve some of the critical problems. The examples of such creative solutions will be discussed in this section.

The most commonly reported solution is the infiltration of sulfur into carbonaceous materials. Such method enhances the conductivity of the electrodes, which otherwise would be pretty poor due to the low conductivity of sulfur. Furthermore, the confinement of sulfur into carbonaceous material is reported to mitigate the dissolution

of polysulfide. The extent of the mitigation depends on the pore size in which the sulfur is confined. In the case of sulfur diffused into pores bigger than 1.2 nm, the dissolution of sulfur still occurs due to the diffusion of electrolyte within the pores which allows the sulfur to react with the li ions. However, the extent of the dissolution is observed to be lower due to the physical barrier that reduces the rate of loss. In the case of sulfur diffused into pores smaller than 1.2 nm, electrolyte is unable to diffuse into such pores due to the steric hindrance. It is widely reported that sulfur confined in such small pores are able to react with li ions through desolvation and the solid state diffusion of li ions. In this case, the polysulfide dissolution is effectively minimized, demonstrating little or no loss of capacity during the extended cycles. Various types of carbon have been reported to be useful for the mitigation of the dissolution of polysulfide. The reported carbon includes, microporous carbon, mesoporous carbon, hierarchical porous carbon, carbon black, hollow carbon, multi-walled carbon nanotube, carbon nanofibers, and graphene [10]. Aside from carbonaceous materials, metal oxides and chalcogenides have been suggested to minimize dissolution. Although, such materials have low conductivity, the chemical polarity of the structure allows the chemically adsorption of polysulfides. Other ideas suggested include polymer composites of sulfur materials. The composites of sulfur with polyacrylonitrile, polypyrrole, and polyaniline have been tested using various synthesis procedures.

A configurational change to the cell has been also tried to reduce the dissolution of

polysulfide. Most widely reported methods are interlayers, which are inserted between the cathode and the separator as a physical barrier against the polysulfide dissolution. Usually carbonaceous materials are used as the interlayer due to its high surface area, which increases the chance of capturing polysulfide lost from the cathode. The critiques of this method often point out that the insertion of an interlayer between the cathode and the separator reduces the overall volumetric and gravimetric energy density of the cell. However, there is no doubt that the method is an efficient barrier against the polysulfide dissolution. A similar concept applied to the current collector has been suggested. Examples include 3-dimensional porous current collectors using metal foam, porous carbon, AAO templates, and porous biomaterials, which have been applied and shown to offer better cyclability with a higher sulfur loading than those using aluminum foil as the current collector. Other novel concepts presented include the usage of polysulfide as a catholyte within the Li-S cell. The idea entirely scraps the idea of the mitigation of the polysulfide dissolution. Instead, when catholyte is coupled with an active material with high surface area, the utilization of the catholyte can be maximized. As long as a sufficient amount of polysulfide is supplied to the system, which could make up for the polysulfide lost to the reduction on the lithium metal anode, the system is able to produce high capacity with high efficiency. As can be seen, extensive researches have been done on the polysulfide dissolution.

In contrast, the issue concerning the volume expansion during the reduction of sulfur

is not very well addressed. Although the review papers mention that during the reduction of sulfur to lithium sulfide, the active material experiences 80% of volume expansion, generally, the issue hasn't been well addressed in the papers. Usually, the reduction in cyclic performance is related to the polysulfide dissolution or the production of the side products from the decomposition of electrolyte components. Even in my research, after cycling, the active material is observed with TEM, which confirms that the particles are intact and its structure is not deformed in anyway, confirming the volume expansion is not a major problem. However, since the structural change within the porous carbon hasn't been done, the study on the effect of volume expansion for the sulfur particles during the reduction is inconclusive.

There are few research done on the modification of the lithium metal anode. This is probably due to the reactiveness of the material towards H_2O, which severely limits the extent of the research that can be achievable in academic settings. Despite such difficulties, the improved performance based on the modification of the surface of the lithium metal anode has been achieved and reported in papers [13]. However, much work is still left for further advancement.

The second chapter of the thesis discusses the issues overlooked in using hierarchical porous carbon structures for Li-S battery, which could prove to be pivotal in further advancement of micropore-confined sulfur.

1.3. The objective of the dissertation.

The core of the thesis is the investigation of the electrochemical reactions occurring within the porous carbon structures for the Li-S and Li-ion batteries. In the first part, I have investigated whether the micropore-confined sulfur within hierarchical porous carbon structures are utilized within the conventional voltage range using the generally accepted current density. In the second part, a 3-dimensionally ordered mesoporous carbon with high surface area is used as an anode, and its performance is enhanced through the modification of its SEI layer using a conventionally reported electrolyte additive. Through these findings, I present some very basic principles that have been overlooked in the past, and suggest the need for the change in paradigm regarding the utilization of porous materials for the energy storages.

In the first part, I investigate the electrochemical reactions of micropore-confined sulfur within hierarchical porous carbon structures. Publications are rife with reports that hierarchical porous carbon can improve the electrochemical performance of the composite materials for Lithium-Sulfur batteries. However, to manifest the utilization of both meso- and micropores as originally intended in the material design, a rational and systematic comparison between sulfur confined in micropores and those confined in hierarchical porous structures is still required. Other than mere assumptions of utilization of micro- and mesopores within hierarchical porous carbon through demonstration of improved cyclic performance, specific evidence to prove the full utilization of the pores has yet to be found in previous works.

Small micropore, hierarchical microporous, and mesoporous carbon, each infused with sulfur, are prepared as cathode materials for Lithium-Sulfur batteries and we, for the first time, demonstrate an activation process of micropore-confined sulfur within hierarchical porous structures based on controlled experiments. By systematic comparison of microporous and hierarchical porous structures, we show that at sufficiently low current, sulfur infused hierarchical porous structures display a slowly activated and reversible reaction at 1.75 V vs Li/Li+ during discharge in addition to the conventionally reported two voltage plateau at 2.3 and 2.1 V. The reaction is absent upon cycling simple mixtures of sulfur and hierarchical porous carbon, strongly suggesting the sulfur confined in micropores (due to capillary force during heat treatment) is responsible. The present results highlight the kinetically hindered reaction of micropore-confined sulfur within hierarchical porous carbon, which changes the general paradigm regarding application of hierarchical porous carbon in the Lithium-Sulfur battery. It is our hope that this finding could set new directions for future research regarding the design of more efficient and high performing porous materials for the Lithium-Sulfur batteries.

In the second part, the surface of the 3-dimensionally ordered mesoporous carbon is investigated during the electrochemical reaction and proper modification is made to enhance it lithium ion battery performance. Vinylene carbonate (VC) is a widely reported electrolyte additive for lithium ion batteries that enhances the performance of both cathode and anode materials. It has been reported that the addition of VC alters the

derived SEI properties, improving the cyclability at elevated temperatures, reducing the irreversible capacity, impeding the cointercalation of the solvent molecules, and decreasing the released gases from the decomposition of solvents. While such beneficial roles are well documented, the application of VC in anode materials has been generally limited to graphite. Applications in other carbonaceous materials, such as a porous carbon with high surface area is yet to be investigated. Due to the large number of defects on the surface, the decomposition of electrolytes produces a thick SEI layer, impeding Li ion passage. Thus, the effect of VC derived SEI on the performance of a porous carbon is investigated.

To this end, we synthesized a 3-dimensionally ordered mesoporous carbon (3DOmC) with high surface area, and systematically examined the effect of different concentration of VC and the resulting SEI on the performance of 3DOmC based lithium ion battery. Our findings show that upon addition of 5 wt.% VC, the discharge specific capacity at the 100^{th} cycle increases to 844.3 from 684.3 mAh g^{-1}, a 23.4% increase over that of the standard electrolyte. Moreover, the first cycle's Coulombic efficiency increases to 32.4 from 23.7 %, and the electrochemical impedance spectroscopy reveals that the resistance of VC derived SEI is smaller than that of the standard electrolyte. The present results highlight the effectiveness of VC in improving the performance of a non-graphitic carbonaceous material. This finding could set new directions for future research regarding the applications of VC in enhancing the performance of non-graphitic porous carbons.

Figure 1.6. The pros and cons of the porous carbon structures for applications in Li-ion and Li-Sulfur battery.

Chapter 2. Activation of micropore-confined sulfur within hierarchical porous carbon for lithium-sulfur batteries.

2.1. Introduction

Among various material designs, hierarchical porous structures, consisting of micro- and mesopores, are often thought to improve both specific capacity and rate capability of energy storage materials [10, 14-27]. For instance, in Li ion batteries, numerous papers have reported that mesopores enhance electrolyte diffusion within the pores, whereas micropores significantly increase the surface area and active sites [16, 19-21, 23-25]. Similar material design concepts have been applied to Li-S batteries, wherein in addition to the aforementioned benefits occurring in Li ion batteries, micropores are "designed for encapsulating/immobilizing the active material" [10] to alleviate polysulfide dissolution [28-35], a major problem in Li-S batteries. Such features have been repeatedly mentioned to highlight hierarchical porous carbon structure as an excellent material design.

While rapid improvements in performance using hierarchical porous carbon structures are highly encouraging for Li-S batteries, the complex electrochemical mechanism within the porous structures is yet to be fully understood. For instance,

many research groups have identified that characteristic two voltage plateau at 2.3 and 2.1 V (vs. Li/Li^+) arise from conversion of solid S_8 to soluble polysulfide and then from polysulfide to solid Li_2S, accordingly [10]. However, a question still remains as to whether and how the sulfur confined in micro- and mesopores are utilized.

On a related note, several groups have reported sulfur infused into microporous structures display only a single plateau starting around 1.6~1.8 V [36-38]. Wan et al. reason that small sulfur molecules, S_{2-4}, are confined in small micropores and are free of polysulfide dissolution, hence the omission of first plateau (~2.3 V). Huang et al. further elaborate that solid-solid reactions occur with small micropore-confined sulfur that causes high resistance, resulting in a Li_2S formation reaction occurring below 1.8 V with overpotential [37]. It's more likely that the micropore-confined sulfur has a thermodynamically lower reduction potential. For such reasons, in both cases, the cells are discharged to 1.0 V, applying low current (0.1C) to fully lithiate the micropore-confined sulfur [36, 37]. In contrast, hierarchical porous structures are often discharged to 1.5 V and/or apply 1C [28-33], which are higher and faster than those reported to lithiate micropore-confined sulfur [36-38].

In order to investigate whether the sulfur infused inside micropores within hierarchical porous structures can be utilized as intended, the electrochemical reaction of sulfur infused 1) small micropore carbon (SMC) and 2) hierarchical microporous carbon (HMC) are compared and further corroborated with voltage profiles of sulfur infused 3)

mesoporous carbon (MC). The findings reported in this paper suggest, for a hierarchical porous structure, there exists a kinetic barrier that must be overcome to utilize its micropore-confined sulfur.

2.2. Experimental

2.2.1. Synthesis of resorcinol-formaldehyde (RF) polymer and carbon spheres (SMC)

All the reagents were used in the experiments as received. Generally, 1.42 g of resorcinol (Junsei) and 1.63 g of formaldehyde (Amresco) were mixed with solution containing (200 ml) deionized water (H_2O). Then, 0.7g of ammonia solution (28%, Wako) was added. After stirring for more than 24h in room temperature, the container was moved to an oven and subsequently heated for 24h at 90℃ under a static stirring condition. The solid product was recovered by centrifugation and it washed several times with deionized water. For carbonization process, the RF polymer spheres were heated under N_2 atmosphere at 800℃ for 3h with a heating rate of 4.3°/min. The resulting products were labeled SMC.

2.2.2. CO_2 activation of SMC to obtain HMC

The carbon dioxide activation was performed using 250mg of SMC in alumina boat. SMC in an alumina boat was placed in a quartz tube in the isothermal zone of a tubular furnace and purged with flowing nitrogen. The samples were then heated to the elevated temperature (30℃/min) followed by changing the gas flux to carbon dioxide(1000 cc/min) for 2h. Activated carbon was named HMC.

2.2.3. Synthesis of MC

MC was prepared by using mesoporous silica nanoparticle template. To synthesize mesoporous silica template, 420 g of DI water, 200 g of absolute ethanol (J. T. Baker), 2.22 g of cetyltriammonium bromide (CTAB, 99%, Daejung Chemicals), 6 g of ammonia solution (28~30%, Samchun Chemical), and 4.08 g of tetraethyl orthosilicate (TEOS, ≥ 96%, TCI Chemicals) were mixed and allowed to react for 16 h. Colloidal product of the mixture was washed by repeated centrifugation and re-dispersion in ethanol. The product was dried at 80 ℃ under reduced pressure, and then calcined at 600 ℃ for 3 h in muffle furnace to remove remaining CTAB in mesopores. The mesopores of silica template were filled with carbon source by acid catalyzed gas-phase polymerization of phenol (≥ 99%, Sigma Aldrich) and paraformaldehyde (95%, Sigma Aldrich). In order to decorate acid catalysts on the pore wall, 2 g of silica template was mixed with 2 g of aluminum (III) chloride hexahydrate (99%, Sigma Aldrich) in a co-solvent of 20 mL of ethanol and 20 mL of DI water. Under sonication of the mixture, Al ions were able to be adsorbed on the pore wall. After dried at 80 ℃ under reduced pressure, the product was calcined at 800 ℃ for 3 h in muffle furnace. 2 g of calcined product, 2 g of phenol, and 1 g of paraformaldehyde were located and sealed in glass container. The container was then heated at 100 ℃ for 12 h in an oven to allow gas-phase polymerization. The carbon source containing product was encapsulated by thin silica shell which reduces the inter-particle sintering at the carbonization step. After that, it was carbonized at 800 ℃ for 3 h in Ar atmosphere. Finally, silica template was etched by 6

M KOH solution at 180 ℃ for 16 h. Etched product was fully washed by repeated centrifugation and re-dispersion in DI water until the pH of supernatant reached 7. Additionally, it was calcined at 800 ℃ for 1 h in Ar atmosphere again to remove functional moieties formed by KOH etching on the surface of carbon.

2.2.4. Preparation of carbon-sulfur composites and mixtures

Sulfur (Alfa Aesar) and a corresponding porous carbon (SMC, HMC, MC) were thoroughly mixed in the following mass ratio; $m_s:m_c$ = 50:50 for SMC_17S, $m_s:m_c$ = 67:33 for HMC_40S, $m_s:m_c$ = 70:30 for HMC_50S, $m_s:m_c$ = 72:28 for HMC_65S, and $m_s:m_c$ =50:50 for MC_40S. Each mixture was sealed in a SUS container and heated at 155 ℃ for 6 h and then heated at 300 ℃ to remove excess sulfur. SMC and S Mixture (17 wt.%) was prepared by mixing sulfur and SMC with the same sulfur to carbon weight ratio as that of SMC_17S. HMC and S Mixture (40 wt.%) was also prepared with the same sulfur to carbon weight ratio as that of HMC_40S.

2.2.5. Characterization

X-ray powder diffraction (XRD) was collected using Rigaku (D/MAX 2500) with Cu Kα (λ = 0.15418 nm). The Raman spectra were recorded with a Horiba Jobin-Yvon LabRam Aramis spectrometer with the 514.5 nm line of an Ar ion laser as the excitation source. X-ray photoelectron spectroscopy (XPS) was performed using Sigma Probe

(ThermoFisher Scientific) with Al Kα (1486.6 eV) as the X-ray source. The cycled electrodes were extracted within a glove box and then washed with solvent (DOL:DME) three times, then dried overnight. Afterwards, the samples were transferred into a hermetically sealed vial to a glove box attached to XPS, whereupon the sample was loaded into XPS. Thermo Avantage software was used to fit the raw data with Lorentzian-Gaussian function and smart background. Nitrogen sorption experiment was carried out using BELSORTP-max. SEM images were observed with FE-SEM (SIGMA, CARL Zeiss) and TEM images and EDS were obtained using JEOL EM-2010 microscope at an acceleration voltage of 200 kV. TGA analysis was done in a Nitrogen atmosphere with a temperature ramp of 10 ℃ (TA Instruments TA SDT Q600).

2.2.6. Electrochemical measurements

The active material, super P, and polyvinylidene fluoride (70:10:20) were mixed using n-methyl-2-pyrrolidinone as the solvent. The slurry was pasted on an Al foil via doctor blade method. An active material loading of ~0.5 mg cm^{-2} was used. Lithium foil was used as the anode and the separator was obtained from SK chemical. 1 M LiTFSI in a mixture of DOL and DME (1:1 by volume) with 0.1 M $LiNO_3$ was used as the electrolyte (Panax Starlyte). The galvanostatic cycling was performed using 2032 coin cells and carried out on a WBCS3000 (Wonatech System, Korea). For the galvanostatic intermittent titration technique (GITT), a current pulse of 167.5 mA g^{-1} was applied for 5

min to measure the closed-circuit voltage (CCV) and then turned off for 10 min to measure the quasi-open-circuit voltage (QOCV) (Fig. 2.4). The current density and specific capacity were calculated based on the weight of sulfur. Electrochemical impedance spectroscopy was tested after a period of rest on Zennium (Zahner) in the frequency range from 100 KHz to 10 mHz with an amplitude of 5 mV.

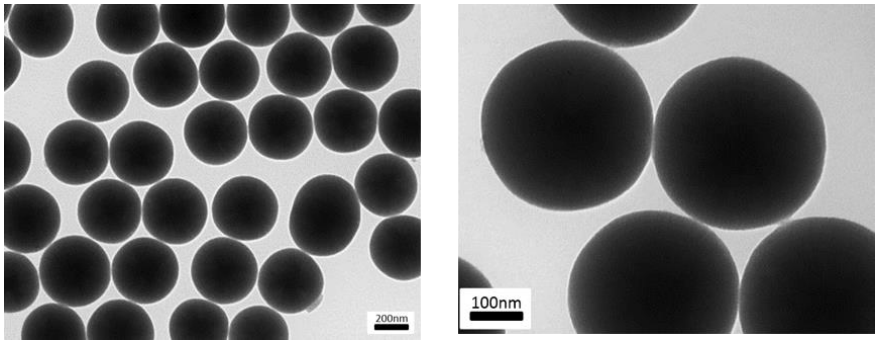

Figure 2.1. TEM images of Mesoporous silica preform for synthesis of MC.

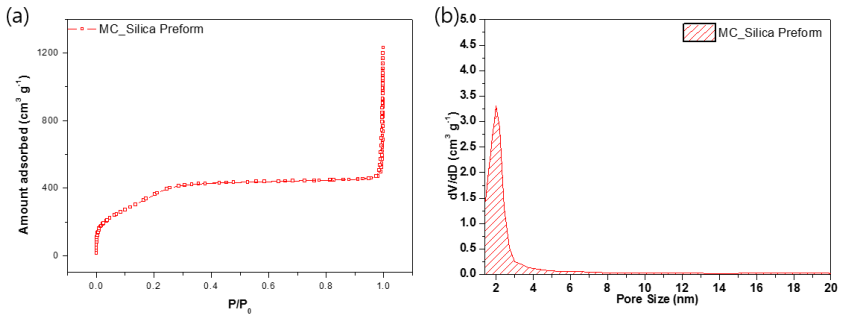

Figure 2.2. Mesoporous silica preform's (a) N2 sorption isotherms and (b) pore size distribution curve using BJH method.

Figure 2.3. The SUS container used for the sulfur infusion.

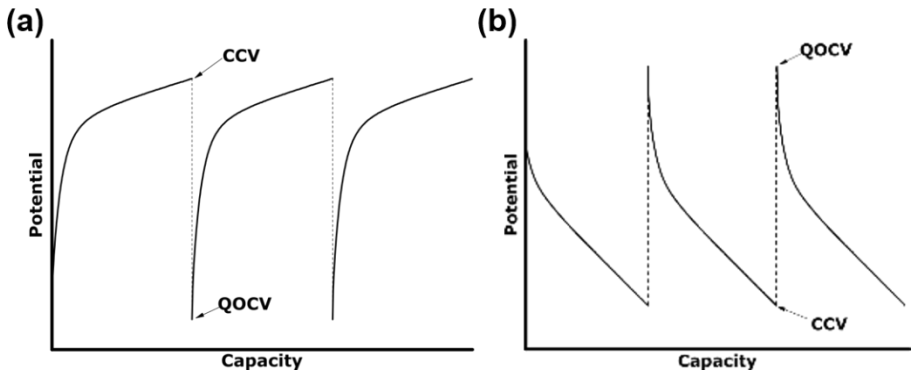

Figure 2.4. Experimental scheme of the GITT profile during the (a) charge and (b) discharge. The absolute value of the potential difference between the CCV and QOCV is used to calculate the internal resistance.

2.3. Results and discussion

As a model system, SMC that is synthesized via carbonization of monodisperse polymer spheres (Fig. 2.5) [39], and HMC whose pore size and surface area are increased via CO_2 activation process using SMC are employed. The SEM and TEM images of SMC and HMC in Fig. 2.6a and c show smooth surfaces and monodisperse particle sizes [40, 41]. XRD analysis shows more featureless pattern of HMC around 24 ° than that of SMC (Fig. 2.7). The increased disorderedness of HMC is confirmed under Raman spectra (Fig. 2.9), in which the ratio of I_D/I_G bands increases from 0.962 to 1.042 after CO_2 activation of SMC [42].

N_2 sorption data shows a typical type I isotherm for SMC (Fig. 2.8a inset), corresponding to microporous features (0.234 $cm^3\ g^{-1}$). In comparison, increased uptake at low pressure for HMC indicates that the microporosity has increased (1.227 $cm^3\ g^{-1}$). Calculated from the density functional theory (DFT) method, SMC contains pores smaller than 1.2 nm, whereas HMC has micropores and mesopores of size up to 4 nm (Fig. 2.8b). Table 2.1 summarizes the textural properties.

The sulfur is infused into carbon samples by heat treatment. TGA data indicates the sulfur content in SMC is ~17% and that in HMC is ~40%, hence referred to as SMC_17S and HMC_40S, respectively (Fig. 2.10). SEM and TEM images reveal sulfur is not concentrated to particular region (Fig. 2.6 b and d), and the XRD patterns shows the crystalline sulfur peaks are missing after the heat treatment (Fig. 2.7). Similarly, Raman

spectra show heat treated samples have no distinct peaks of Sulfur (Fig. 2.9). After the sulfur infusion, the amount of N_2 adsorbed significantly decreases (Fig. 2.11), resulting in reduction of surface area from 604 to 12 $m^2 g^{-1}$ for SMC_17S and from 2882 to 599 $m^2 g^{-1}$ for HMC_40S (Table 2.1). There is a sharp reduction in pore size distribution peaks (Fig. 2.6f) along with total pore volume (Table 2.1).

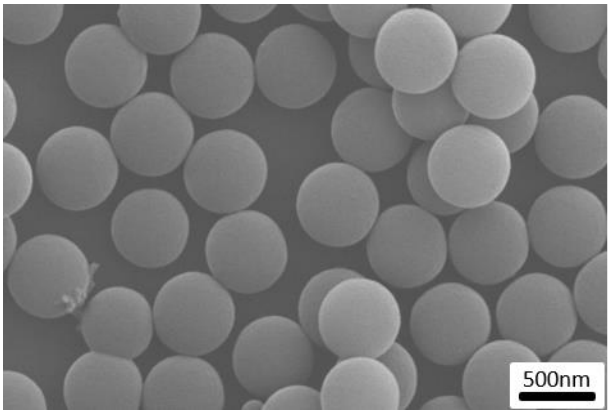

Figure 2.5. SEM image of Resorcinol-Formaldehyde polymer spheres (570± 21 nm) before carbonization to SMC.

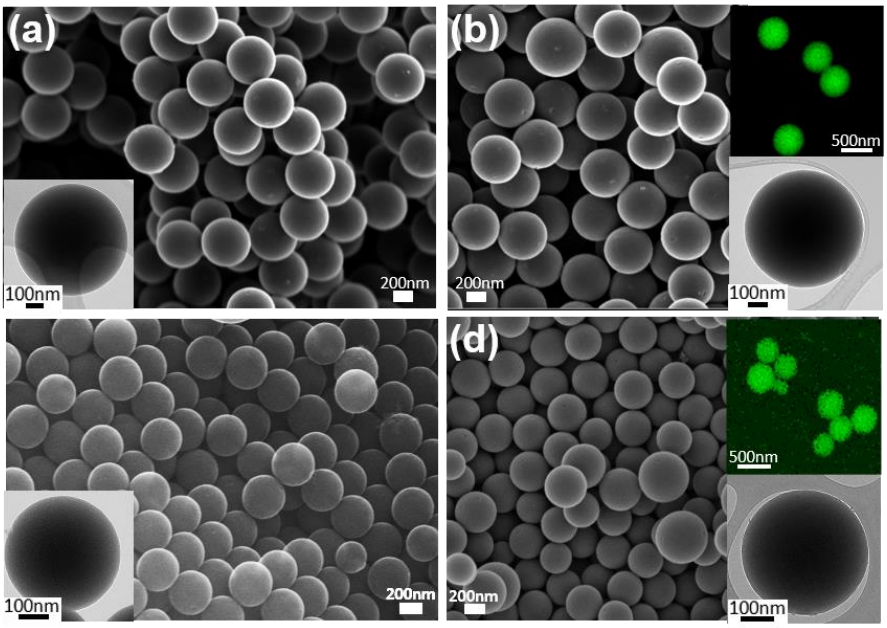

Figure 2.6. SEM images of (a) SMC, (b) SMC_17S, (c) HMC, and (d) HMC_40S (inset: (a-d) TEM images and (b and d) EDX mapping of Sulfur).

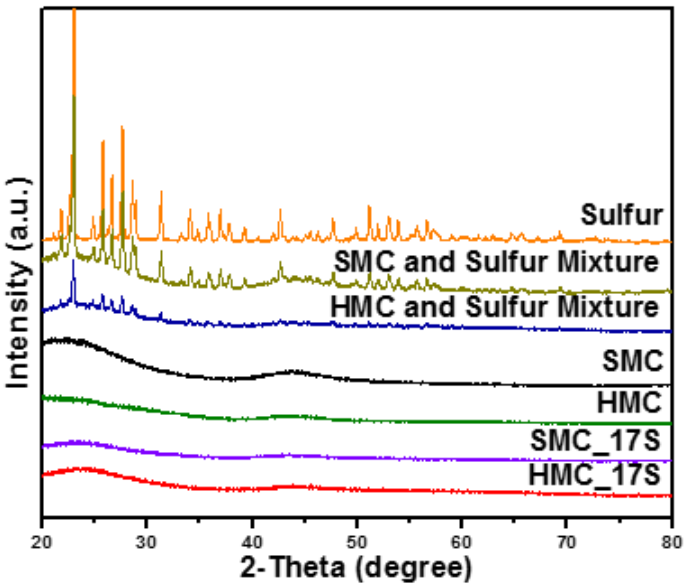

Figure 2.7. X-ray diffraction patterns of samples.

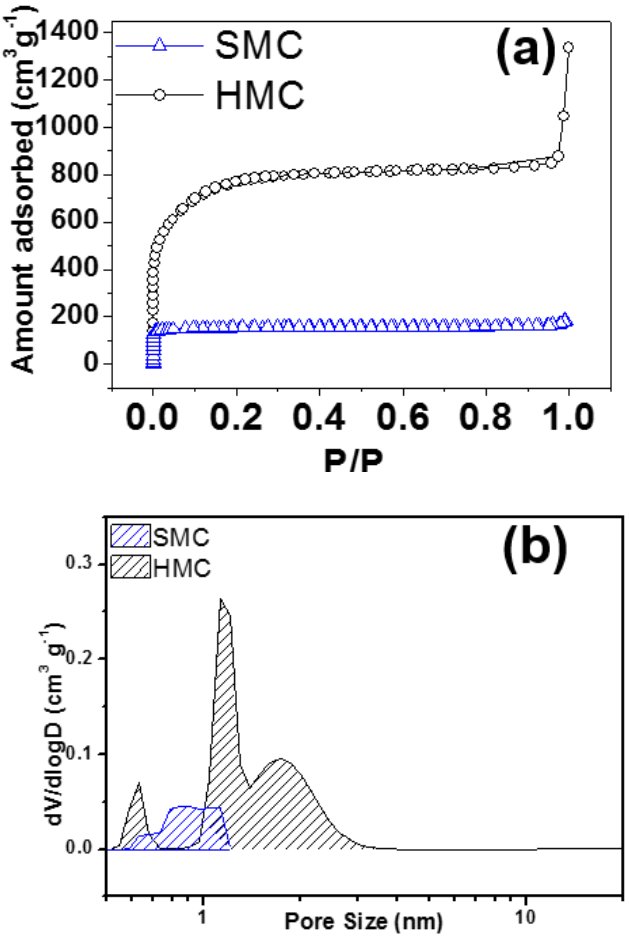

Figure 2.8. (a) N_2 sorption isotherms. (b) Pore size distribution curves of SMC and HMC using the DFT method.

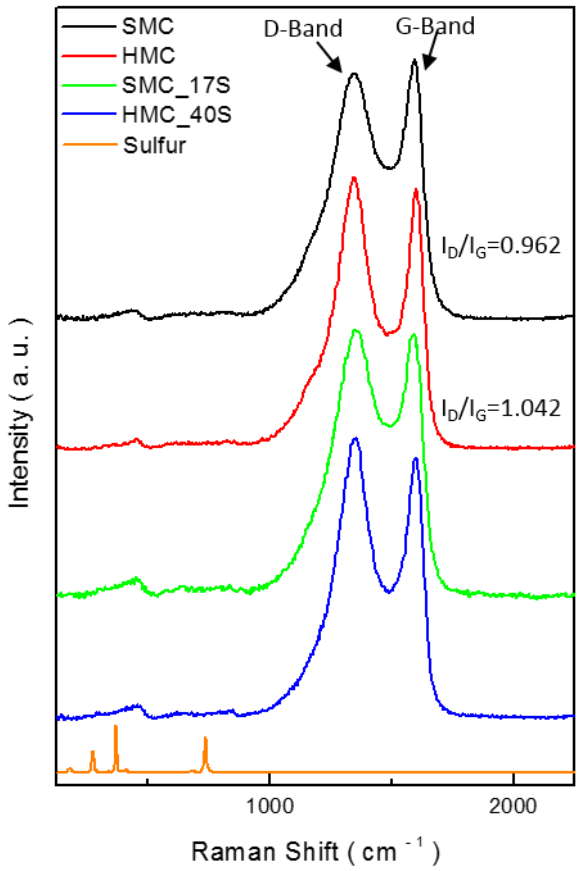

Figure 2.9. Raman spectrum of SMC, HMC, SMC_17S, and HMC_40S.

Samples	Micropore Volume(cm^3/g)	Total pore Volume(cm^3/g)	BET surface area(m^2/g)
SMC	0.234	0.282	604
HMC	1.227	1.720	2882
MC	0.406	1.033	1135
SMC_17S	0	0.033	12
HMC_40S	0.253	0.302	599
MC_40S	0	0.195	63

Table 2.1. Physical properties of SMC, HMC, MC, SMC_17S, HMC_40S, and MC_40S. Micropore volume and BET surface area are calculated using the t-plot method and Brunauer-Emmett-Teller model, accordingly.

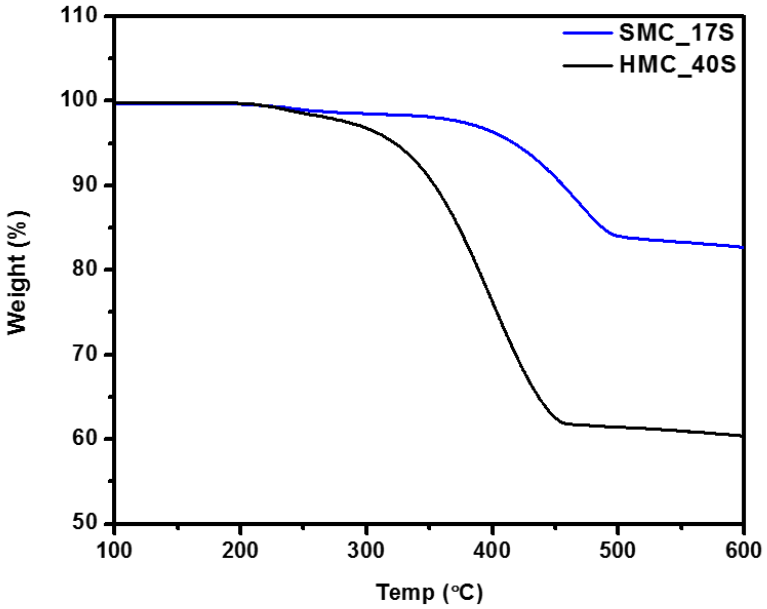

Figure 2.10. TGA curve of SMC_17S and HMC_40S in N_2 atmosphere.

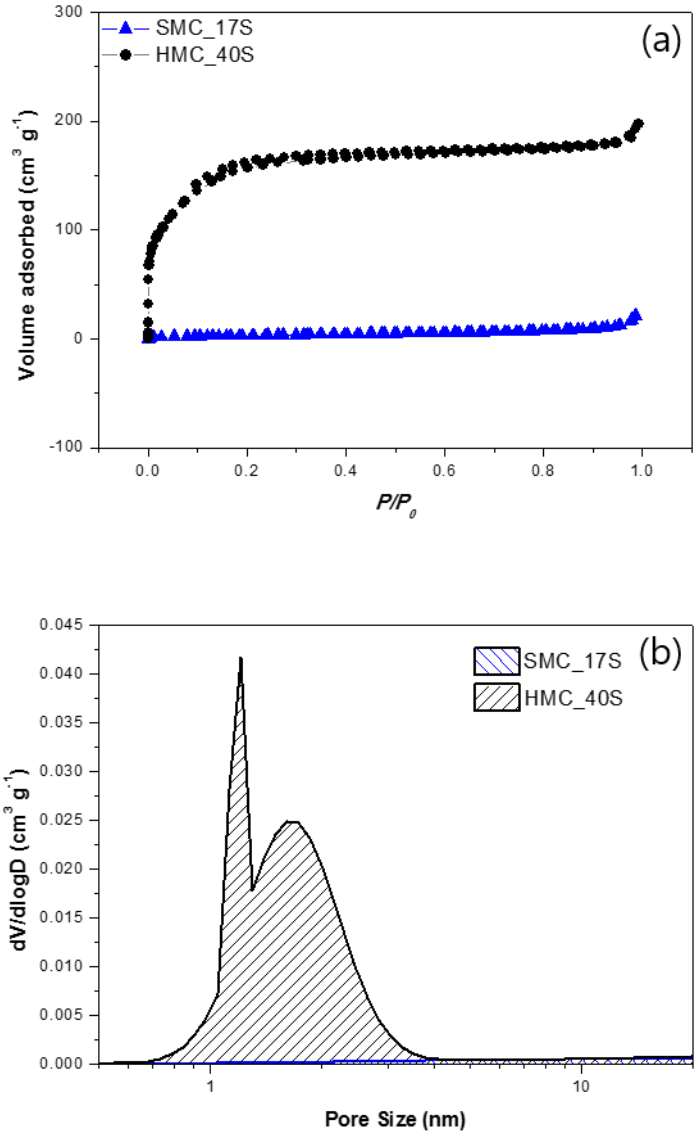

Figure 2.11. (a) N_2 sorption isotherms of SMC_17S and HMC_40S and (b) pore size distribution of SMC_17S and HMC_40S.

SMC_17S is cycled at 0.1C between 1 and 3 V, and the resulting voltage profile shows a single plateau with large irreversible capacity at the 1st discharge (Fig. 2.12a). The large irreversible capacity results from interfacial charge storage [43]. From the 2nd cycle and onwards, only a single plateau is observed at 1.75 V, because the solvent molecules are sterically hindered due to the size of micropores (<1.2 nm for SMC). Therefore, solid state diffusion of Li ions into micropore-confined sulfur is suspected to have occurred, resulting in the absence of the first plateau related to dissolution of polysulfide and instead resulting in the presence of the second plateau with large overpotential [36, 37]. While the cyclability of SMC_17S is excellent (923 mAh g^{-1} at 200th cycle) (Fig. 2.12b), the pore volume is limited to incorporate large amounts of sulfur (~25% max, taking into account volume expansion of Li_2S) and electrolyte within the pores.

On the contrary, HMC has a larger pore volume for loading sulfur (~ 66.5% max). At first, HMC_40S is cycled at 1C, the current of choice for testing hierarchical porous structures [28-30], between 1 and 3 V (Fig. 2.13). In contrast to SMC_17s, there are two plateaus at discharge. The first plateau at 2.3 V arise due to the dissolution of polysulfide, probably from larger pores (>1.2 nm), enabling solvated Li ions to diffuse in and react with sulfur [37]. The dissolved polysulfide then finally converts to Li_2S during the second plateau shown at 1.9 V.

Likewise, in the case of cycling at 0.1C, initially we observe similar plateaus (Fig. 2.14a). However, beginning on the 5th cycle, a third plateau is observed starting at ~1.5 V

at discharge. The plateau continuously shifts to higher voltage with further capacity as the cycle goes on, eventually reaching 1.75 V with 870 mAh g^{-1} on the 50^{th} cycle. The dQ/dV plot clearly shows the shift to higher potential along with an increase in peak intensity (Fig. 2.14b). During the charge, the peak around 2.6 V is continuously shifted to lower potential along with an increase in peak intensity (Fig. 2.14c). Such results indicate that in addition to the widely reported two voltage plateaus at the discharge, there exists a third plateau, which is gradually activated only upon cycling at slow current with sufficiently low cut-off voltage. The reaction is kinetically hindered, but is reversible once activated. The potential and the shape of the third plateau are very close in resemblance to those of SMC_17S. Such similarities point to the possibility that micropore-confined sulfur within HMC_40S may induce such a phenomenon.

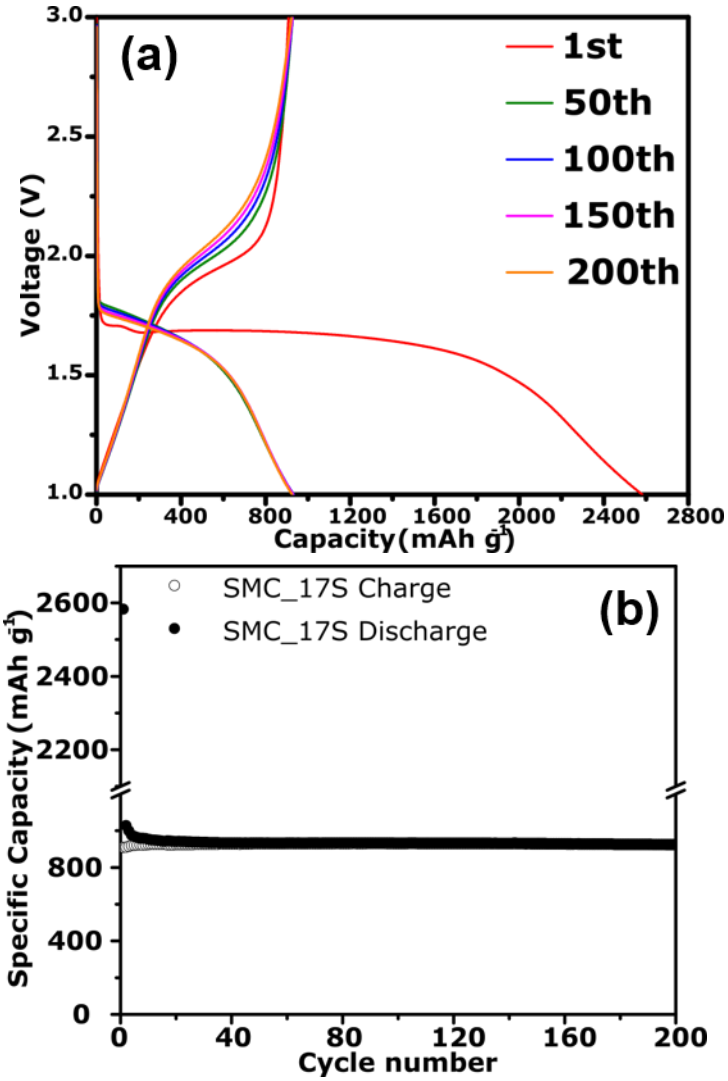

Figure 2.12. Voltage profiles of (a) SMC_17S cycled at 0.1C and (b) the cyclic performance for 200 cycles.

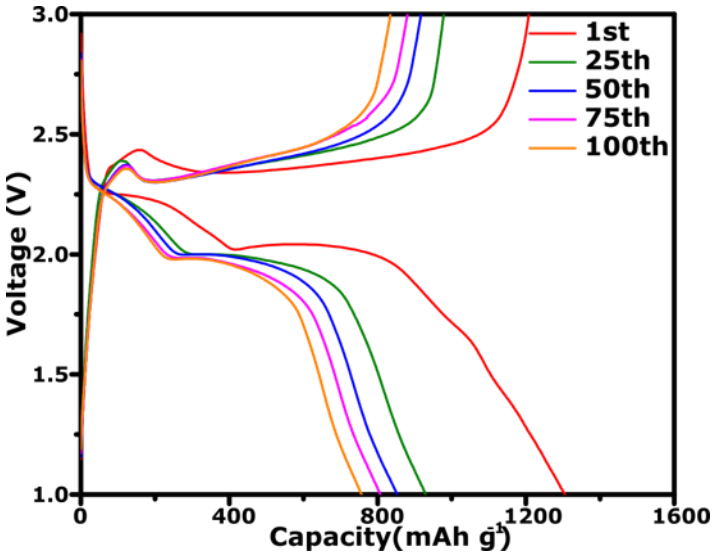

Figure 2.13. Voltage profiles of HMC_40S cycled at 1C.

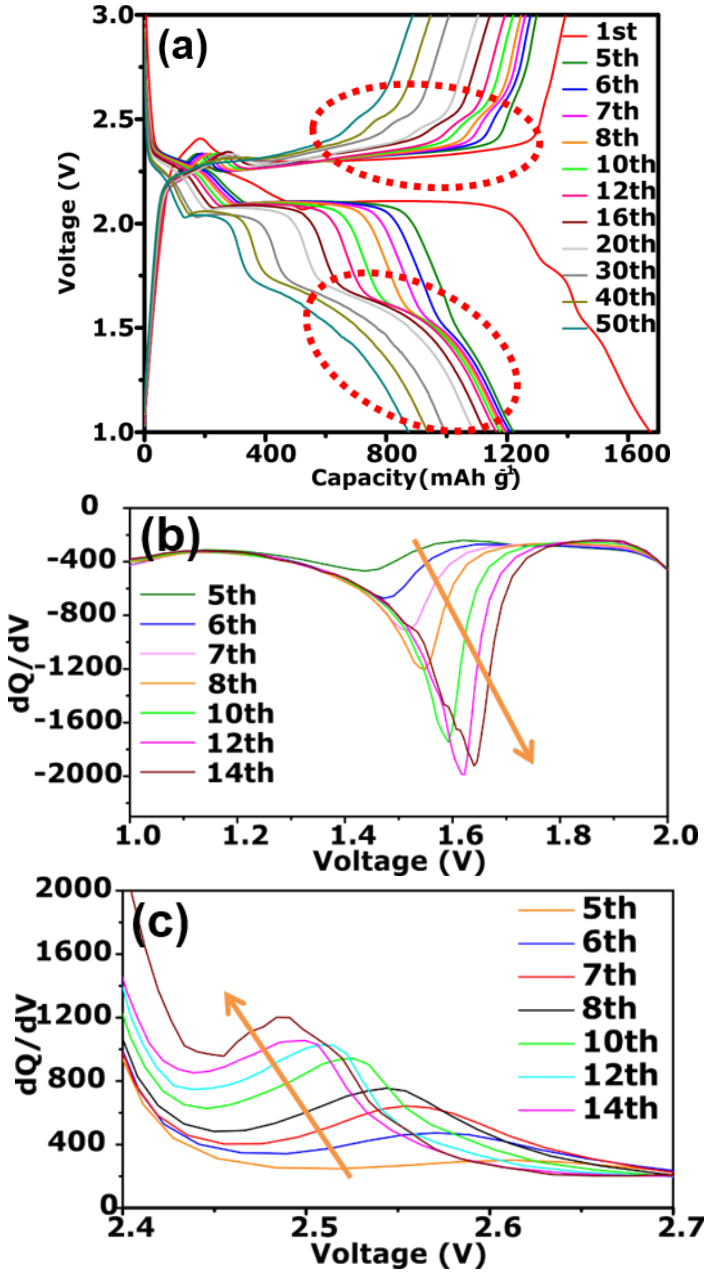

Figure 2.14. Voltage profiles of HMC_40S cycled at (a) 0.1C. dQ/dV plot of HMC_40S cycled at 0.1C during (b) discharge and (c) charge.

For verification, SMC and HMC are each mixed with sulfur in the amount corresponding to SMC_17S and HMC_40S and cycled to observe their voltage profiles (Fig. 2.15a and b). In contrast to their thermally treated counterparts, the mixed samples show only two voltage plateaus. These results indicate simple particulate interactions between porous carbon and sulfur do not create reactions in the voltage plateau at 1.75 V. Rather, the sulfur confined in pores due to capillary force during the heat treatment is likely responsible [44].

To further verify the existence of inactive micropore-confined sulfur within HMC_40S, ex situ X-ray photoelectron spectroscopy (XPS) is employed. S_{2p} spectra of pristine electrode, and cycled electrodes after discharge (3 and 15 cycles) are analyzed, and the corresponding percentages of S-S bond are 63.7, 14.4, and 8.7 % (Table 2.2). Despite discharging to 1.0 V at 0.1C for 15 cycles, the S-S doublet peaks are still visible (Fig. 2.16a). The detection of S-S bond from the surface of electrodes (~5 nm depth), strongly suggests there remains inactive sulfur, most likely from those confined in micropores.

The change in the internal resistance is measured with the GITT experiment on the 125^{th} cycle (Fig. 2.17). During the discharge, the internal resistance at 1.5 V is more than twice that of 2.1 V (Fig. 2.18a). Likewise, during the charge, high internal resistances are observed at 2.3 and 2.6 V (Fig. 2.18b). The former is due to the overpotential required to oxidize and dissolve Li_2S [45], whereas the latter is related to the activation process. The high internal resistance during the activation reaction

corroborates that the reaction is kinetically limited due to the solid state diffusion of Li ions.

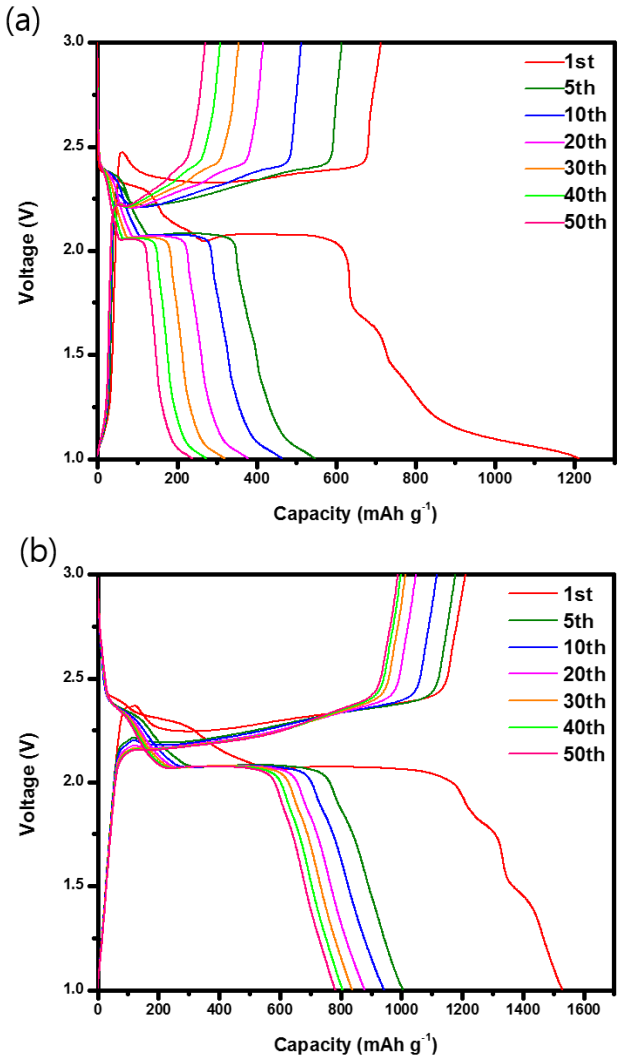

Figure 2.15. Voltage profiles of (a) SMC and S Mixture (17 wt.%) and (b) HMC and S Mixture (40 wt.%) @ 0.1C.

Band	Binding Energy	HMC_40S Pristine (%)	HMC_40S 3 Cyc Discharged (%)	HMC_40S 15 Cyc Discharged (%)
S-O (-SO_4)[1,2,3,4]	170.5 169.3	36.3	29.9	36.5
S-O (-SO_3)[1,2,3,4]	168.2 167.2		32.7	42.4
S-S[1,2,3]	165.0 163.9	63.7	14.4	8.7
Li-S (Li_2S-S^*O_3)[1,2,3,4]	163.0 162.0		23.0	12.4

Table 2.2 Assignments for peaks in the S_{2p} spectrum and the corresponding content analysis of sulfur containing species in the cathodes before and after cycling.

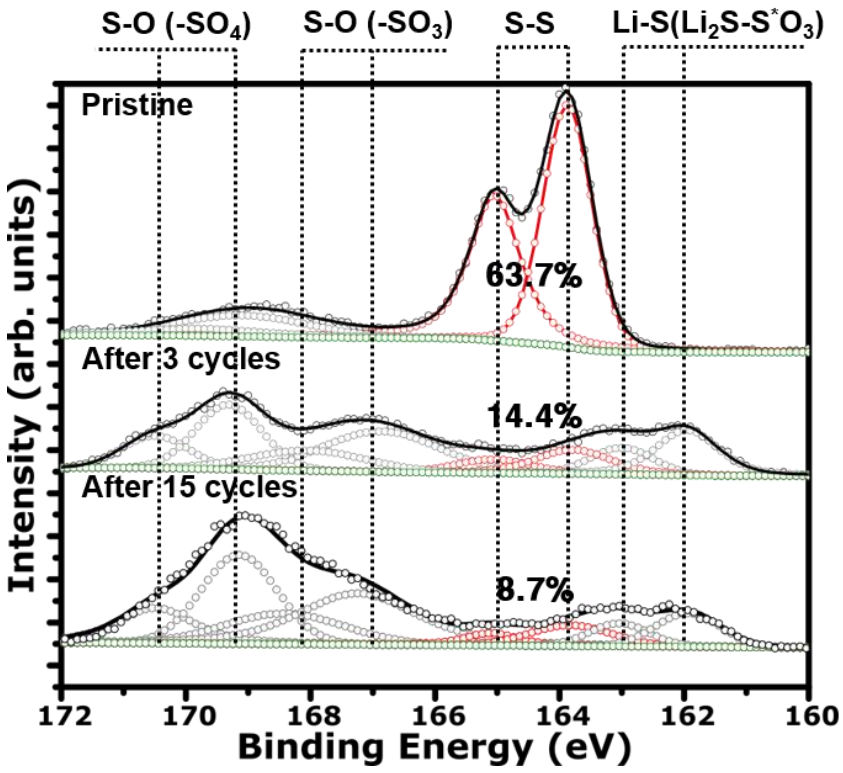

Figure 2.16. (a) S2p XPS spectra of HMC_40S before and after discharge.

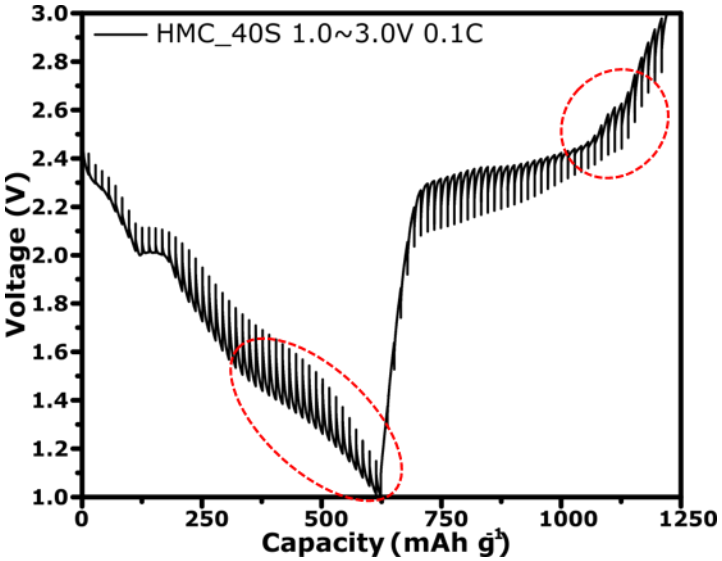

Figure 2.17. GITT voltage profile of HMC_40S cycled at 0.1C on the 125th cycle.

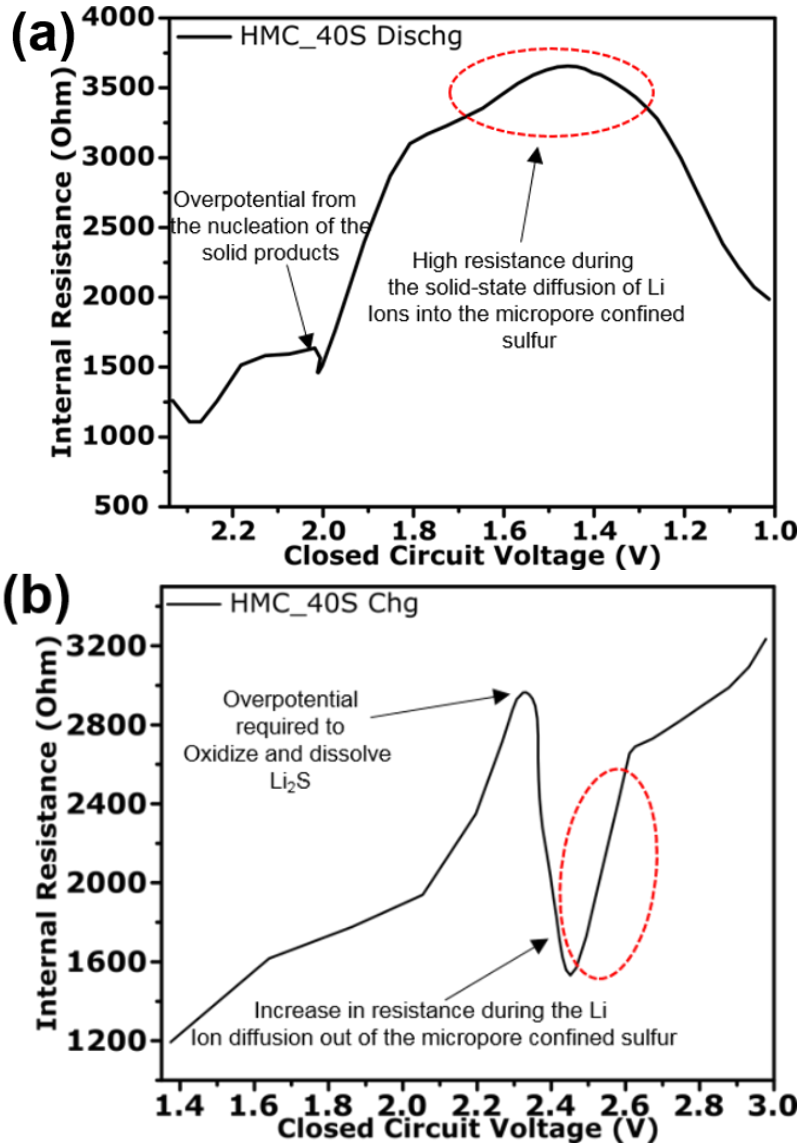

Figure 2.18. The internal resistance calculated from GITT during (c) discharge and (d) charge.

The $LiNO_3$ decomposition on the system is investigated using the cells with the discharge cut-off voltage set to 1.8 and 1.0 V. $LiNO_3$ is known to decompose below 1.8 V as evident from the two little steps shown below 1.8 V in the first discharge (Fig. 2.14a) [46-48]. The impedance of the sample with the cut-off voltage set to 1.8 V remains nearly constant as the cycle goes on, whereas the impedance of the sample with the cut-off voltage set to 1.0 V continuously increases (Fig. 2.19a and b). The increase in impedance is consistent with the increase in overpotential observed at the voltage plateaus of 2.3 and 2.1 V along the cycles (Fig. 2.14a). However, in the case of the plateau observed below 1.8 V, the overpotential is reduced during the early cycles (Fig. 2.14b). The opposite trends in the change of overpotential can be explained upon further examination with TEM images. Side products are found on the surface of HMC spheres when discharged to 1.0 V, whereas the surface remains relatively pristine when discharged to 1.8 V (Fig. 2.21). XPS indicates that the large percentage of side products are Li_XSO_y (Table 2) [49], which we suspect are the islands formed on the surface and confirmed by the EDS data (Fig. 2.12). These side products cause the increase in the overall impedance of the electrode leading to the increase in the overpotential observed at 2.3 and 2.1 V. However, the side products do not completely cover the surface of the HMC spheres, which enables electrolyte to diffuse into the pores and activate the micropore-confined sulfur. As the cycle progress, however, the activation process is overturned and slowly diminished from the 60^{th} cycle and onwards (Fig. 2.20a and 2.23).

The cyclic performance of cells with the cut-off voltage set at 1.8 and 1.0 V are shown in Fig. 2.20b. The cell with the cut-off voltage set at 1.0 V displays more capacity initially due to the deep discharge that utilizes more of the sulfur confined in the porous structures, including the micropore-confined sulfur. As the cycle continues, however, the impedance due to the side products increases and decays the performance. Eventually, the performance of the cell with the cut-off voltage set at 1.8 V supersedes that of the cell with the cut-off voltage set at 1.0 V.

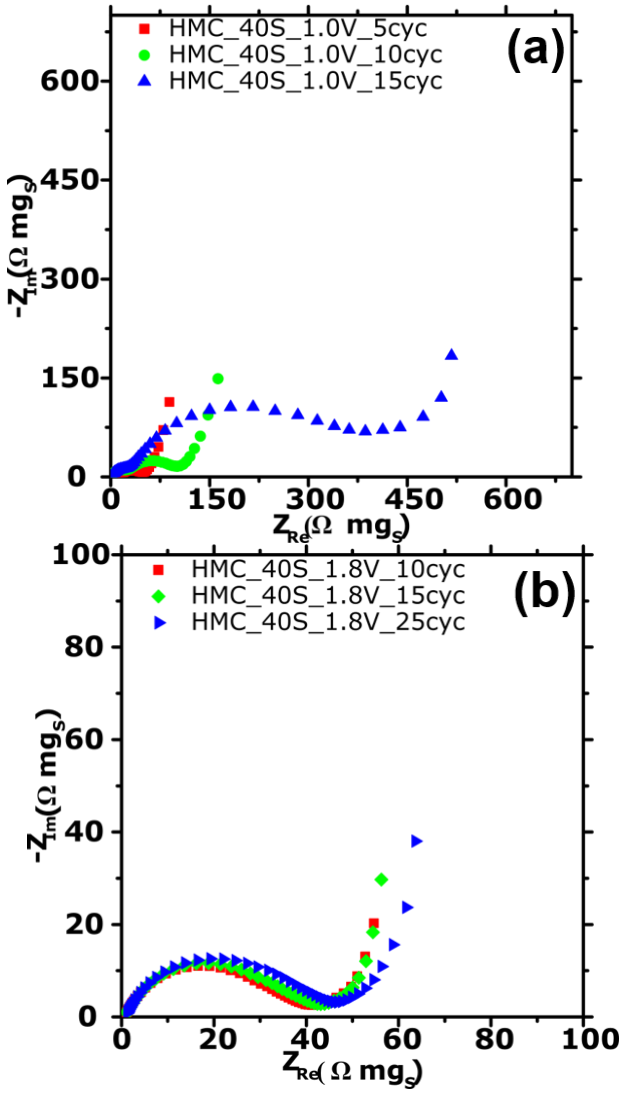

Figure 2.19. The change in the impedance of HMC_40S with the discharge cut-off voltage set to (a) 1.8 V, and (b) 1.0 V along the cycles.

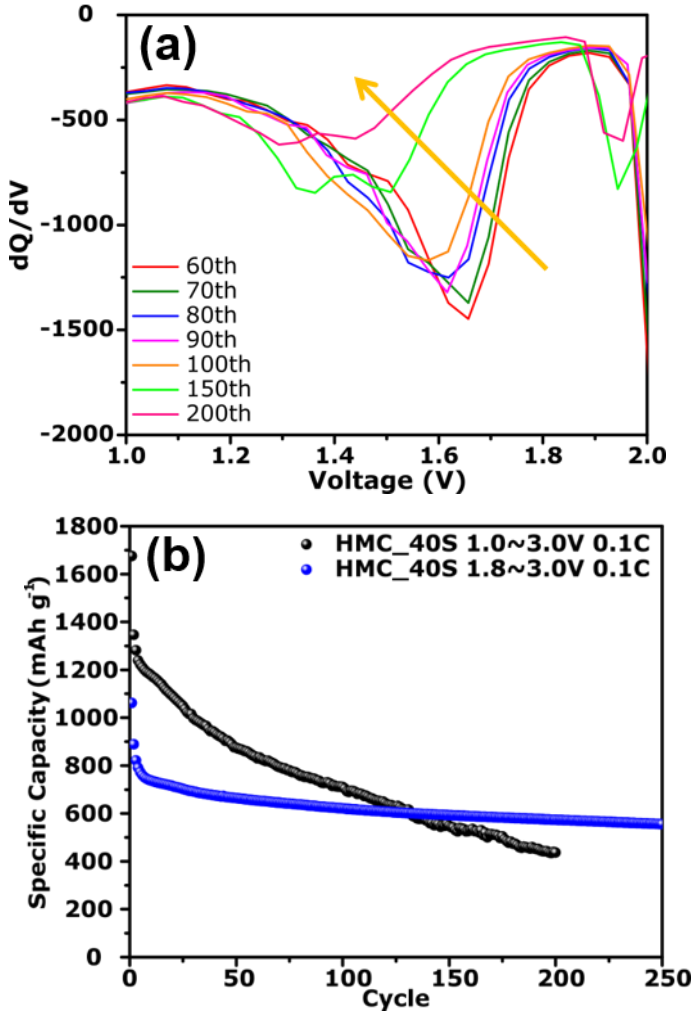

Figure 2.20. (a) dQ/dV plot of HMC_40S cycled at 0.1C during the discharge from the 60th cycle and onwards. (b) Cyclic performance of HMC_40S with the discharge cut-off voltage set to 1.8 V and 1.0 V.

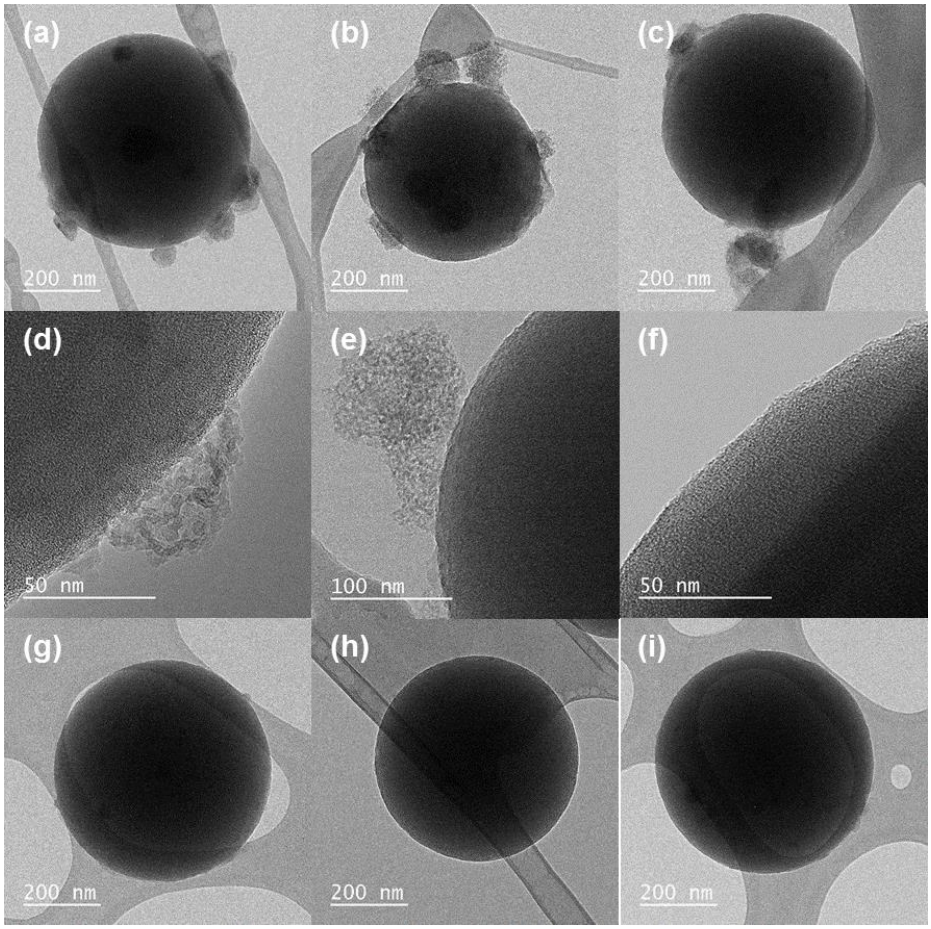

Figure 2.21. TEM images of HMC_40S (a-e) after discharging to 1.0 V for 15 cycles and (f-i) after discharging to 1.8 V for 20 cycles.

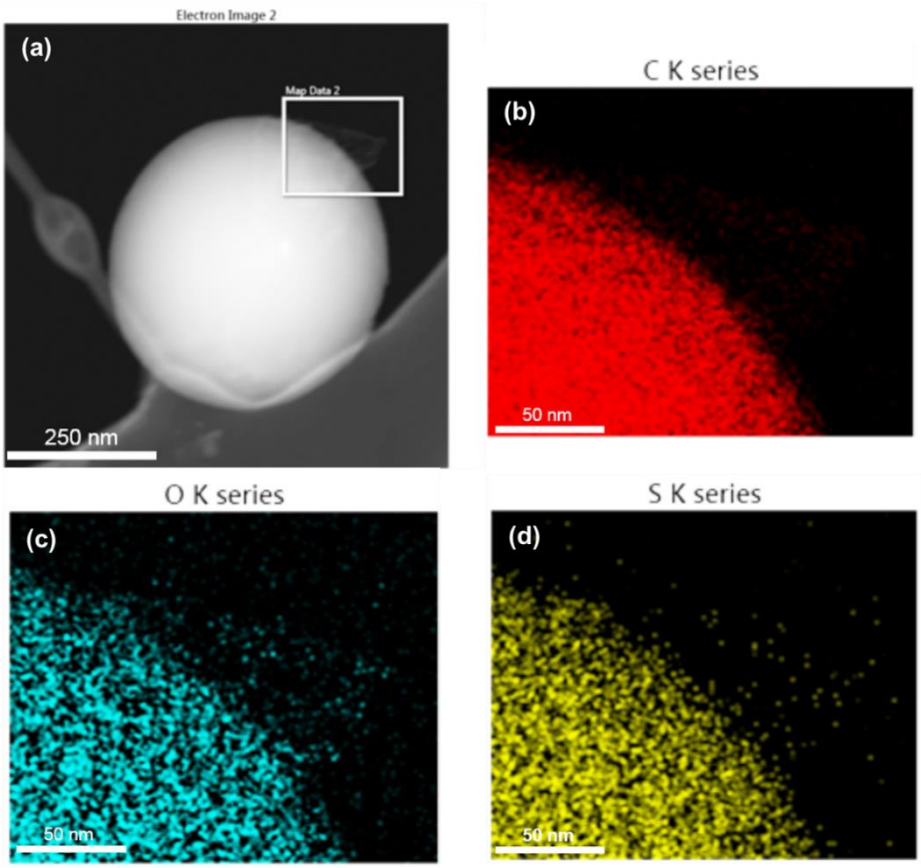

Figure 2.22. (a) HAADF image and (b-d) EDS of the islands of side products formed on the surface of HMC_40S after discharging to 1.0 V for 15 cycles.

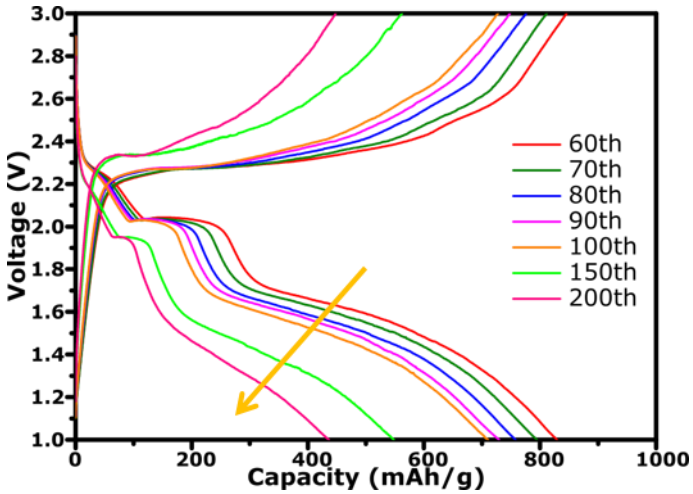

Figure 2.23. The voltage profiles of HMC_40S from the 60th cycle and onwards.

As a final confirmation, a mesoporous carbon (MC) is selected to verify the existence of activation process [40, 50]. MC shows combined N_2 sorption isotherms consisting of type I and IV isotherm, indicating well-developed micro- and mesoporous structures (Fig. 2.24). Its textural properties are summarized in Table 2.1. Sulfur is infused into the porous structure (Fig. 2.25) in similar fashion to that of HMC. TGA confirms the sulfur content is ~40% (Fig. 2.26), hence referred to as MC_40S. MC_40S exhibits the gradual activation of micropore-confined sulfur as well while the MC and S Mixture (40 wt.%) does not (Fig. 2.27). The activation is not as conspicuous as those of HMC_40S, possibly due to a relatively smaller micropore volume (0.406 cm^3 g^{-1} < 1.227 cm^3 g^{-1}). However, the gradual activation is unmistakably visible during both discharge and charge in the dQ/dV plot (Fig. 2.27c and d). The result reconfirms the presence of the activation process regarding micropore-confined sulfur.

The question still lingers as to the mechanism behind the activation process. When the amount of infused sulfur in HMC increases to 50 and 65% (Fig. 2.28), the activation process is delayed and the degree of activation also decreases (Fig. 2.29). The sulfur loading seems to have a direct relationship with the kinetic barrier associated with the activation of micropore-confined sulfur. During the electrochemical reaction, the infused sulfur in meso- and large micropores first converts to soluble polysulfide (2.3 V), which then turns into Li_2S (2.1 V). While sulfur infused into meso- and large micropores has direct access to electrolyte and is kinetically favorable, the sulfur infused

in small micropores which must receive Li ions through solid state diffusion is kinetically hindered and requires thermodynamically lower potential (1.75 V) for the reaction to occur. As the amount of sulfur increases, the amount of polysulfide produced from meso- and large micropores increases as well, inducing a thicker layer of Li_2S which form along the walls of pores that harbor small micropores. As a result, formation of Li_2S, known for low Li ion diffusivity and electronic conductivity [51], worsens the Li ion diffusion into small micropores that confine sulfur, resulting in the presence of inactive micropore-confined sulfur even after discharging to 1.0 V. However, as the cycle goes on, the formation of Li_2S is reduced. This is evidenced by the continuous decrease of voltage plateau at 2.1 V (Fig. 2.14a). This loss is mainly caused by polysulfide dissolution as evident from an increase in color stains of separators along the cycles (3, 15, 50 cycles) for HMC_40S (Fig. 2.30). Once the Li_2S layer induced Li ion diffusion resistance is sufficiently decreased, the micropore-confined sulfur within HMC_40S is gradually activated and its reaction voltage at 1.75 V is observed. The illustration shown in Fig. 2.31 depicts the process.

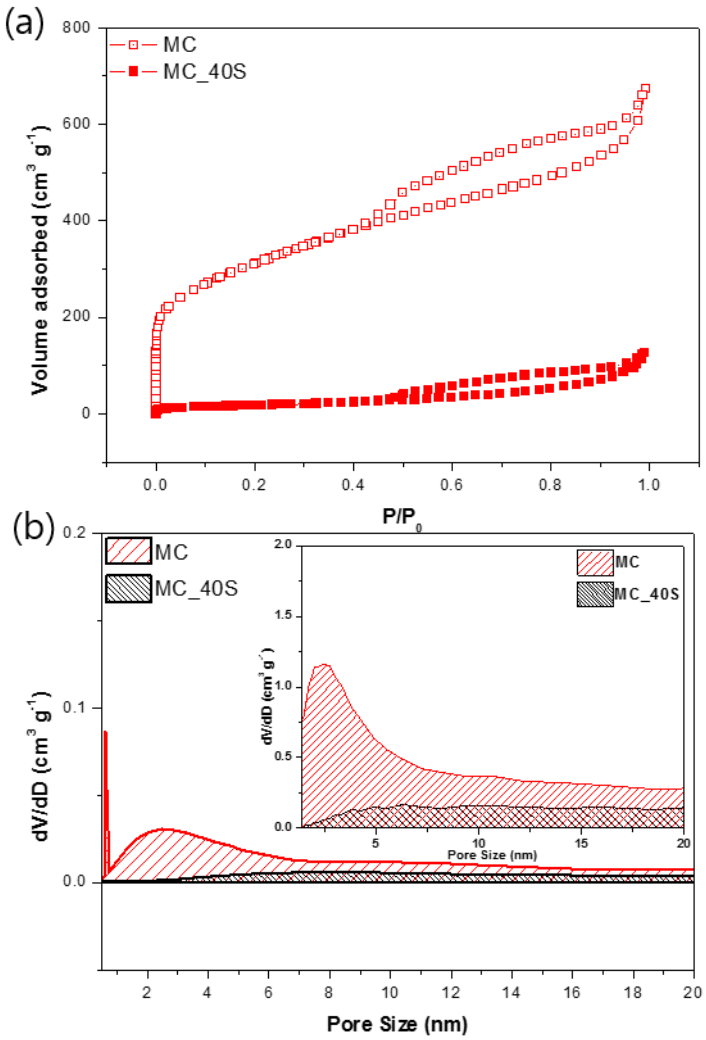

Figure 2.24. MC and MC_40S's (a) N_2 sorption isotherms and (b) pore size distribution curves using DFT method. (inset: Pore size distribution using BJH method).

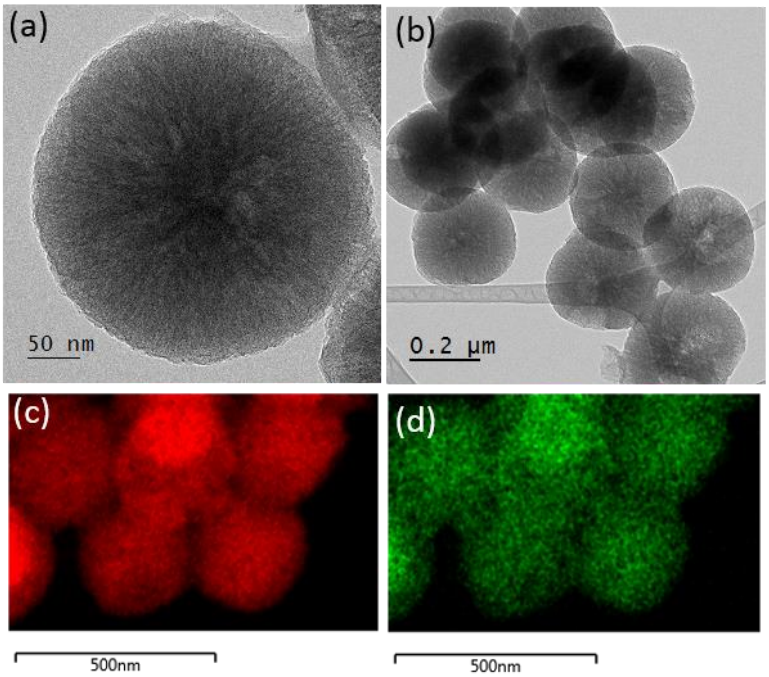

Figure 2.25. (a),(b) TEM images of MC_40S and EDS mapping of MC_40S for (c) carbon and (d) sulfur.

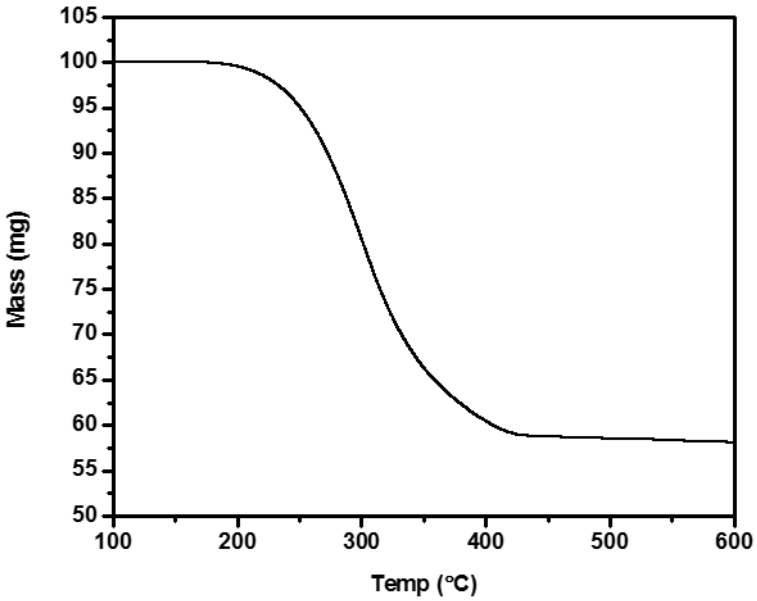

Figure 2.26. TGA curve of MC_40S in N_2 atmosphere.

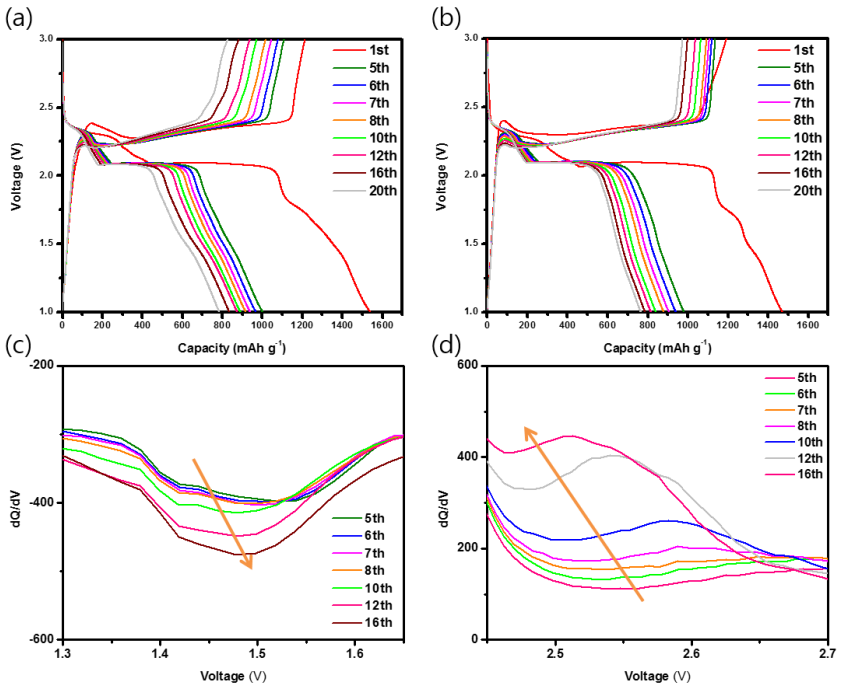

Figure 2.27. Voltage profile of (a) MC_40S and (b) MC and S Mixture (40 wt.%) @ 0.1C and dQ/dV plot of MC_40S for (c) discharging and (d) charging.

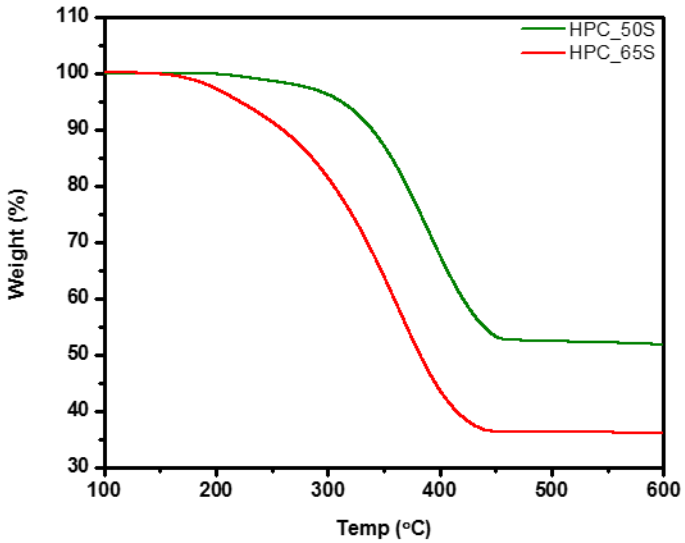

Figure 2.28. TGA curve of HMC_50S and HMC_65S in N_2 atmosphere.

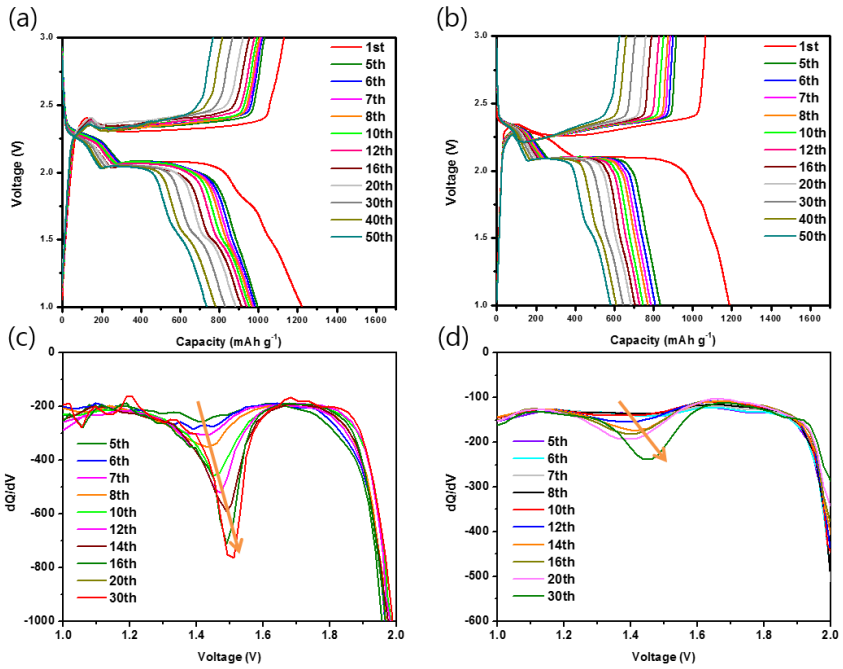

Figure 2.29. Voltage profile of (a) HMC_50S and (b) HMC_65S @ 0.1C and dQ/dV plot of (c) HMC_50S and (d) HMC_65S during discharge.

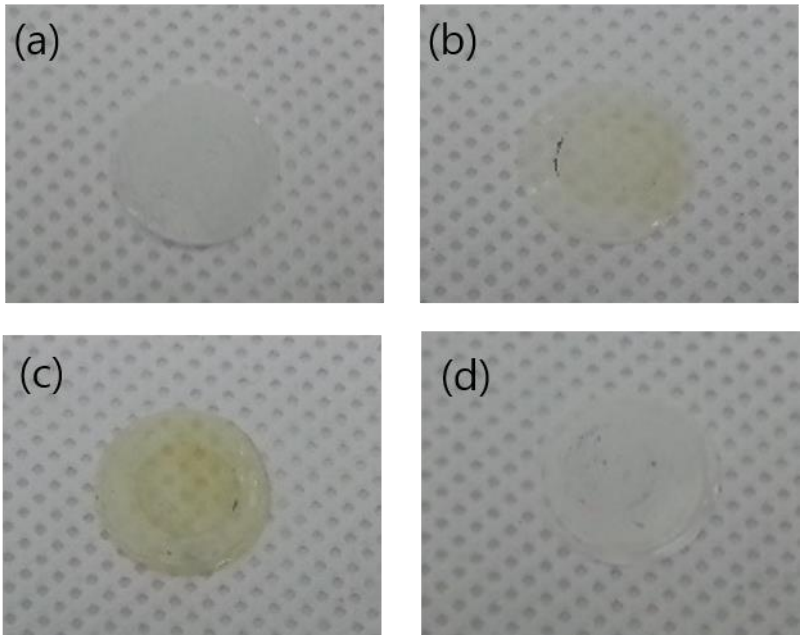

Figure 2.30. The separator extracted from HMC_40S cell after (a) 3 cycles, (b) 15 cycles, (c) 50 cycles, and (d) the separator extracted from SMC_17S cell after 50 cycles.

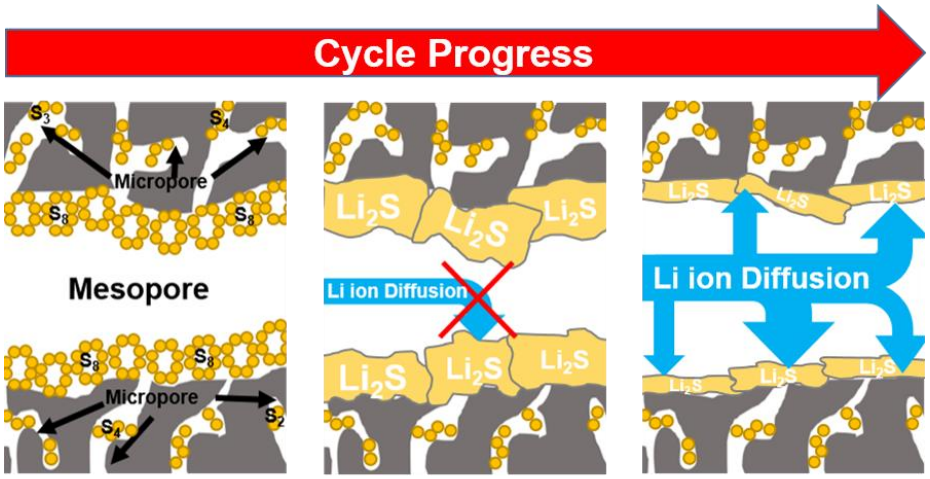

Figure 2.31. Scheme of the proposed mechanism regarding the activation of micropore-confined sulfur within hierarchical porous carbon along the cycles.

2.4. Conclusion

This research, for the first time, demonstrates the activation process of micropore-confined sulfur within hierarchical porous carbon and elaborates on the electrochemical mechanism occurring during the activation process. The voltage profiles of SMC_17S, HMC_40S, and MC_40S are compared to reveal the gradual activation process, supported by the XPS and GITT analysis. Moreover, the effect of $LiNO_3$ decomposition on the activation process is revealed to be minimal early on, but in the long term causes enough resistance to deactivate the process. The cause of the activation process is linked to the kinetic barrier associated with Li ion diffusion through Li_2S layers on the walls of mesopores, where micropore-confined sulfur resides. In view of numerous works associated with applications of hierarchical porous carbon for Li-S batteries [10, 28-33], this work unveils the electrochemical mechanism for micropore-confined sulfur within hierarchical porous structures and sets the foundation for new research opportunities for more efficient utilization of micropore-confined sulfur.

Chapter 3. Improved Electrochemical Performance of a Three-Dimensionally Ordered Mesoporous Carbon Based Lithium Ion Battery Using Vinylene Carbonate.

3.1. Introduction

Vinylene carbonate (VC) is a commonly used electrolyte additive, which is reported to improve the properties of the solid electrolyte interface (SEI) formed on the surface of the electrodes [52, 53]. The properties of the SEI are known to be critical to the performance of the lithium ion battery [53, 54]. When VC is used in a lithium ion battery, it is reduced prior to other electrolyte solvents and creates an improved SEI layer. The resulting positive effect includes the reduction of an irreversible capacity [53, 55-57], the suppression of cointercalation of solvents [58, 59], and the improvement of the cycling performance at elevated temperatures [55, 56, 59, 60]. While the improvement has been reported in both cathodes and anodes [61-63], generally the enhancement has been mainly attributed to the graphite negative electrode [58, 59, 62-65]. The effect of VC derived SEI on other carbonaceous materials, such as a porous carbon with a high surface area, has not been investigated for lithium ion batteries. Due to the large number of defects, porous carbon with a high surface area often shows a large irreversible capacity, resulting in the production of a thick SEI layer, which impedes Li ion diffusion [66, 67]. Therefore,

the properties of SEI layer are critical to the performance of the porous carbon based lithium ion battery.

Herein, we report on the improved Coulombic efficiency and the enhanced discharge capacity of a 3-dimensionally ordered mesoporous carbon (3DOmC) based lithium ion battery at room temperature using VC. A VC concentration that induces the formation of an optimal SEI is identified, and the underlying mechanisms of the improvement in performance are investigated. The properties and the morphology of the VC induced SEI are confirmed using an ex-situ X-ray photoelectron spectroscopy (XPS), electrochemical impedance spectroscopy (EIS), and transmission electron microscopy (TEM).

3.2. Experimental

3.2.1. Synthesis of silica nanoparticles

Monodisperse silica nanoparticles were produced by the modified Stöber method that utilized L-lysine as a catalyst [68]. First, L-lysine monohydrate (80 mg) was dissolved in water (70 g) and subsequently tetraethyl orthosilicate (TEOS, 5.3 g) was added to the bottle. The bottle was closed and then heated to the 90 ℃ under vigorous stirring for 48 h. In order to reach the particle size of around 25 nm, additional amount of TEOS of 10.6 g was used for the seeded growth process for another 48 h. Three-dimensionally ordered silica nanoparticle arrays were produced by evaporation of water in an oven at around 80 ℃ for 24 h. The close-packed silica nanoparticle arrays were calcined at elevated temperature (600 ℃) for 6 h to remove the L-lysine molecules adsorbed on the surface of the silica nanoparticles.

3.2.2. Synthesis of three-dimensionally ordered mesoporous carbon

Three-dimensionally ordered mesoporous carbon (3DOmC) was synthesized by infiltration of furfuryl alcohol to the close-packed silica nanoparticle arrays [69]. Mixture of furfuryl alcohol of 12 g and oxalic acid (60 mg) served as a catalyst was prepared under vigorous stirring for 5-10 min, then the solution was used for the impregnation of silica nanoparticles for several times. The excess of the solution was then removed by the filter paper and the polymer@close-packed silica nanoparticle array was then thermo-polymerized at 90 ℃ for 24 h. Then, the composite was carbonized under inert condition

(N_2) at 800 ℃ for 6 h. Finally, the silica/3DOmC composite was washed with 6 M KOH solution in order to remove silica nanoparticles at room temperature for 2-3 days. The resultant 3DOmC was then obtained with several times of silica etching steps and through washing with water to remove residual KOH solution.

3.2.3. Electrolytes

The standard electrolyte (SE) used for the electrochemical test of 3DOmC was 1 mol L^{-1} of $LiPF_6$ in a mixture of EC and DMC (1:1 by volume) (Panax Starlyte). 5, 10, and 20 wt.% of vinylene carbonate (Aldrich) were added to the SE, and they are referred to as 5VC, 10VC, and 20VC, respectively.

3.2.4. Electrochemical measurements

3DOmC, super P, and polyvinylidene fluoride in a weight ratio of 8:1:1 were mixed with n-methyl-2-pyrrolidinone as the solvent. The slurry was pasted on an Al foil via the doctor blade method. Lithium foil was used as the anode, and a separator from SK chemical is used. The galvanostatic cycling was performed using the 2032 coin cells and carried out on a WBCS3000 (Wonatech System, Korea) at a rate of 100 mA/g with a cutoff voltage of 3.0-0.001 V vs Li/Li^+ at room temperature. EIS was tested after a period of rest on Zennium (Zahner) in the frequency range from 100 KHz to 10 mHz with an amplitude of 5 mV.

3.2.5. Characterization

The SEM images were observed with a SIGMA (CARL Zeiss) and the TEM images were obtained using a Tecnai F20 (FEI). The small-angle X-ray scattering (SAXS) measurement was taken on a SmartLab (Rigaku) using Cu Kα radiation (45kV, 200mA). X-ray powder diffraction (XRD) was collected using a D/MAX 2500 (Rigaku) with Cu Kα (40 kV., 200 mA). The Raman spectra were recorded with a Horiba Jobin-Yvon LabRam Aramis. Nitrogen sorption experiment was carried out using BELSORP-max. Barrett-Joyner-Halenda (BJH) and the density functional theory (DFT) method are used to calculate the mesopores' and micropores' size distribution, respectively. XPS analysis was performed using a Sigma Probe (ThermoFisher Scientific) with Al Kα (1486.6 eV) as the X-ray source. The cycled electrodes are extracted within a glove box, washed with the solvent (DMC), then dried overnight. Afterwards, the samples were transferred directly into XPS.

3.3. Results and discussion

3DOmC is prepared by the infiltration of furfuryl alcohol to the close-packed silica nanoparticle arrays. The SEM and TEM images confirm the well-ordered morphology of the 3DOmC (Fig. 3.1a-e), in which the TEM image shows the pore size is around 23.0±2.5 nm (Fig. 3.1e). According to the SAXS pattern, it shows resolved diffraction peaks around 0.27 nm^{-1} and 0.5 nm^{-1}, indicating the regularity of the structure in the long range (Fig. 3.2). The wide angle XRD pattern shows a broad (0 0 2) and (1 0 0) peak, indicating the carbon is amorphous (Fig. 3.3a). The Raman spectrum further confirms the amorphous nature of the material with the I_D/I_G ratio of 0.887 (Fig. 3.3b). N_2 sorption isotherms are measured to evaluate the textural properties of the carbon (Fig. 3.4). The analysis shows a type IV isotherm, indicating that of mesoporous structure with a total pore volume of 3.84 $cm^3\ g^{-1}$ and a BET surface area of 1229.7 $m^2\ g^{-1}$. Moreover, the DFT analysis (Fig. 3.4 inset bottom) indicates that the micropore volume is minuscule, and the BJH method shows that the size of mesopores is around 21.3 nm (Fig. 3.4 inset top), which corroborates the result from the TEM image.

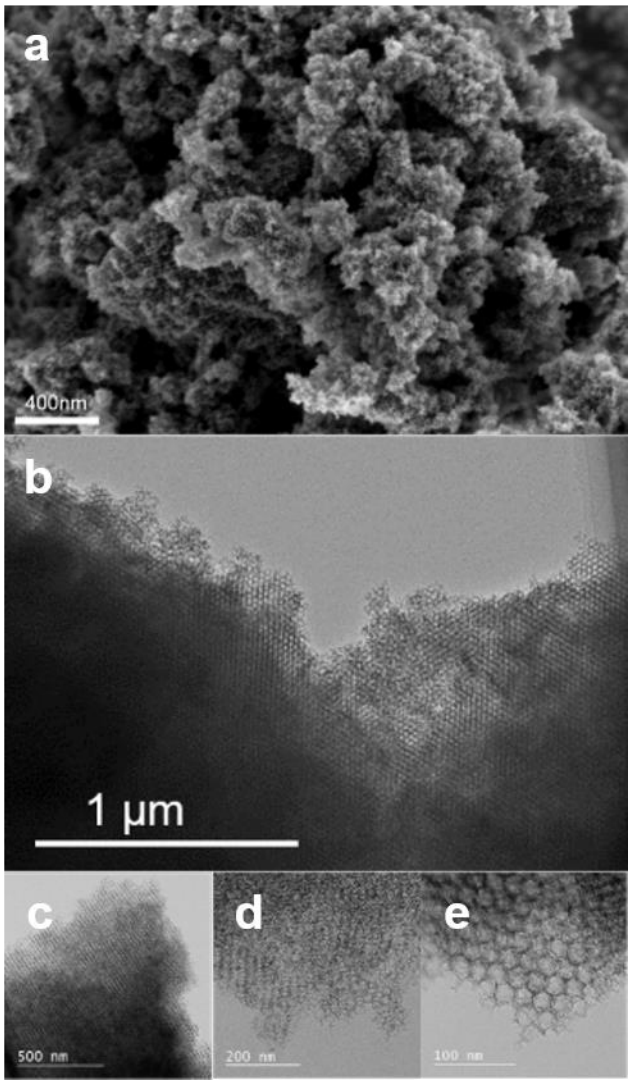

Figure 3.1. (a) SEM and (b~e) TEM images of 3DOmC. (f) SAXS pattern, (g) Wide-angle XRD pattern (inset: Raman spectrum), and (h) N2 sorption isotherm of 3DOmC (inset: Pore size distribution using the BJH and DFT method).

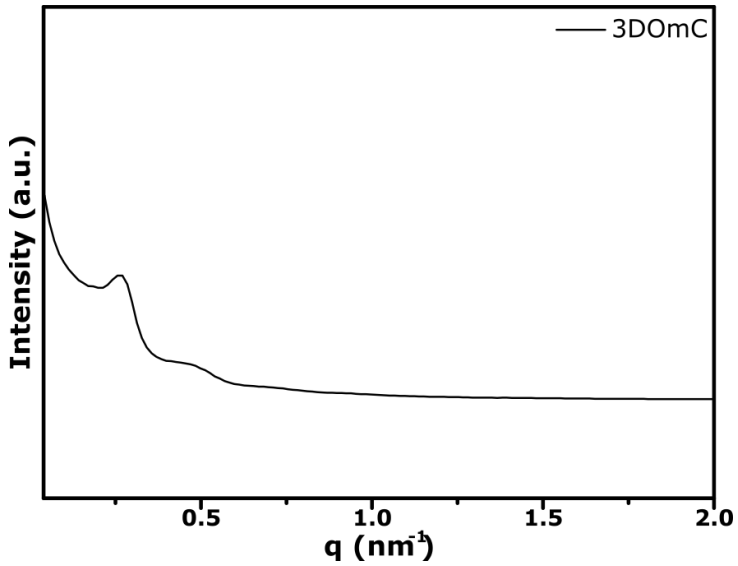

Figure 3.2 SAXS pattern of 3DOmC

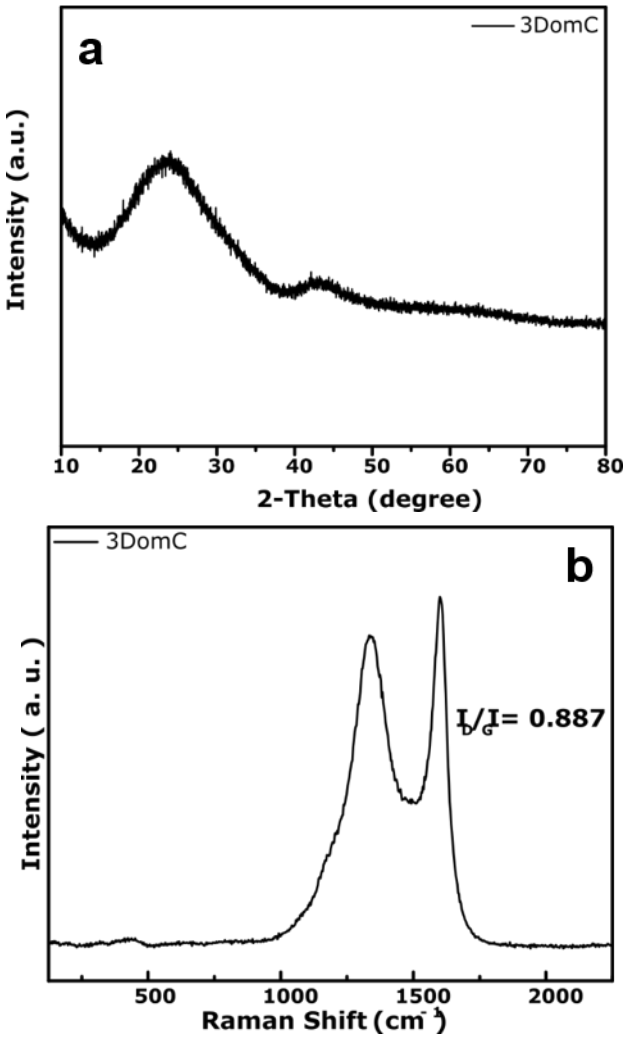

Figure 3.3 (a) Wide-angle XRD pattern and (b) Raman spectrum of 3DOmC.

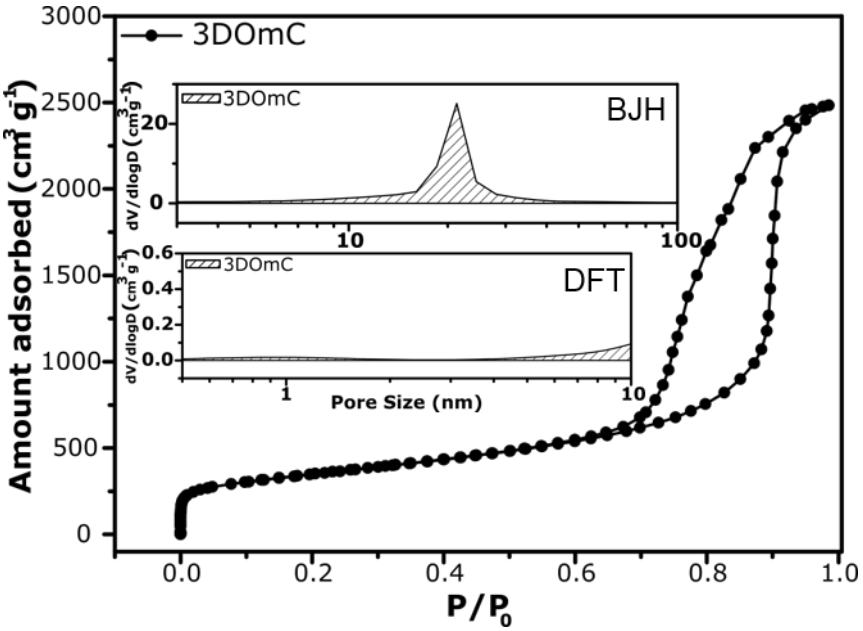

Figure 3.4. N2 sorption isotherm of 3DOmC (inset: Pore size distribution using the BJH and DFT method).

Fig. 3.5 shows the improvements in Coulombic efficiency upon additions of VC in the electrolyte. 5VC, in particular, effectively increases the Coulombic efficiency to 32.4 from 23.7% at the first cycle. Although, 10 and 20VC also increase the coulombic efficiencies to 33.6 and 36.3%, respectively, the increase is not as dramatic as that of the 5VC. The voltage profiles during the first cycle are compared between the different electrolytes (Fig. 3.6). Upon addition of VC, a reductive reaction appears between 1.0 and 1.75 V. The degree of the reductive reaction increases as the amount of VC in the electrolyte increases. Furthermore, the reduction of VC occurs prior to the electrochemical reduction of the electrolyte solvent shown below 1.0 V for SE, confirming the preformation of an SEI layer [59, 62].

The EIS analysis is performed after the first discharge (Fig. 3.7). The SEI and charge transfer resistance are calculated using the circuit shown in the Fig. 3.7 inset. The EIS spectrum consists of two semicircles and a tail, where the diameter of the semicircle in the low frequency represents the charge transfer resistance, whereas the diameter of the semicircle in the high frequency represents the SEI resistance [70]. The result shows that the SEI and charge transfer resistance of SE are 79.1 and 71.4 Ω mg, respectively, but decreases to 68.1 and 25.0 Ω mg in the case of 5VC. In contrast, the SEI and charge transfer resistance of 10VC are increased to 174.6 and 253.0 Ω mg, respectively.

The morphology of the SEI layer in each electrolyte sample is confirmed using a TEM (Fig. 3.8 a-i). In contrast to that of pristine sample (Fig. 3.8 a-c), the SEI layer formed on SE and 5VC can be easily identified (Fig. 3.8 d-i). Although the presence of

SEI layer makes it hard to clearly identify the pores, the difference in contrast still exists where the pores are located. The TEM images show, however, no clear distinction between the SEI Layer of SE and 5VC (Fig. 3.8 d-i). In the case of 10VC, however, the porous carbon structure is clearly covered with a thick SEI layer (Fig. 3.2 j-l), obscuring the identification of the ordered mesoporous structure, which is consistent with the EIS result. Thus, 5VC is chosen as an optimal additive sample due to its effectiveness in increasing the coulombic efficiency and producing a SEI layer with a reduced charge transfer and SEI resistance.

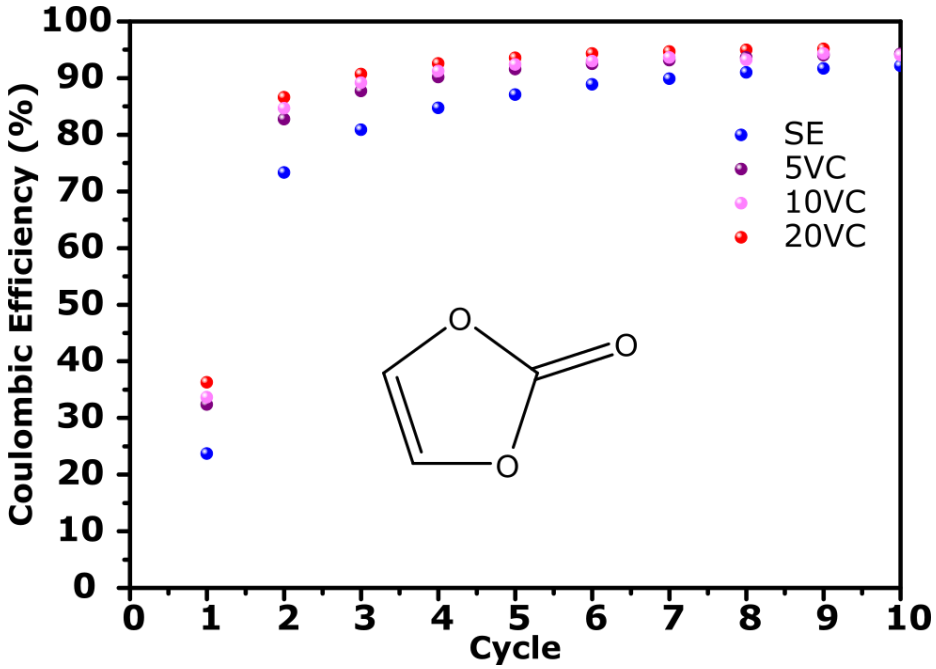

Figure 3.5. Coulombic efficiencies of samples with SE and 5, 10, and 20 wt.% of VC included in SE during the 10 cycles (inset: chemical structure of VC).

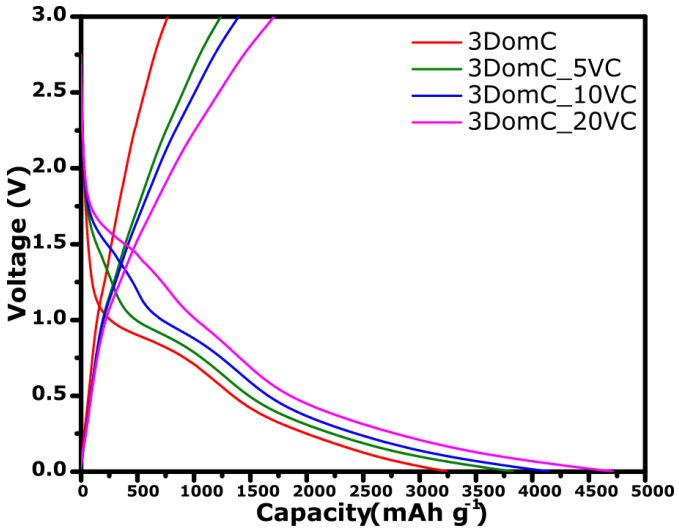

Figure 3.6. The voltage profiles of the samples with SE and 5, 10, and 20 wt.% of VC included in SE samples during the 1st cycle (100 mA/g).

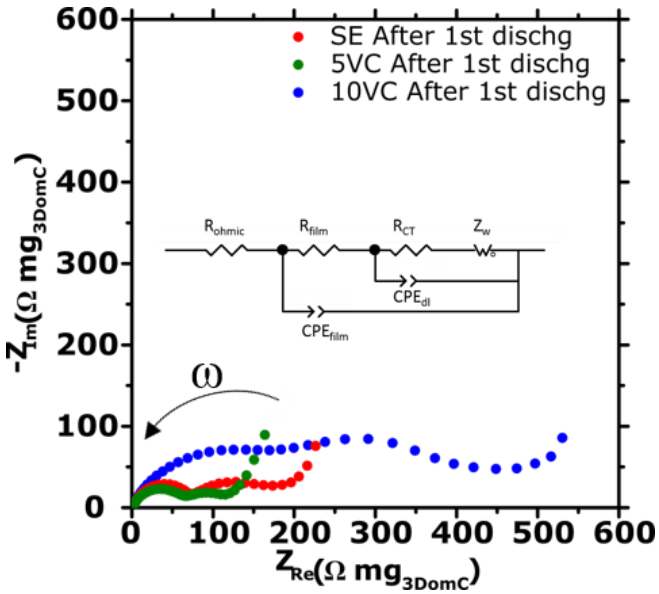

Figure 3.7. EIS data obtained after the 1st discharge (inset: equivalent circuit used to fit the data).

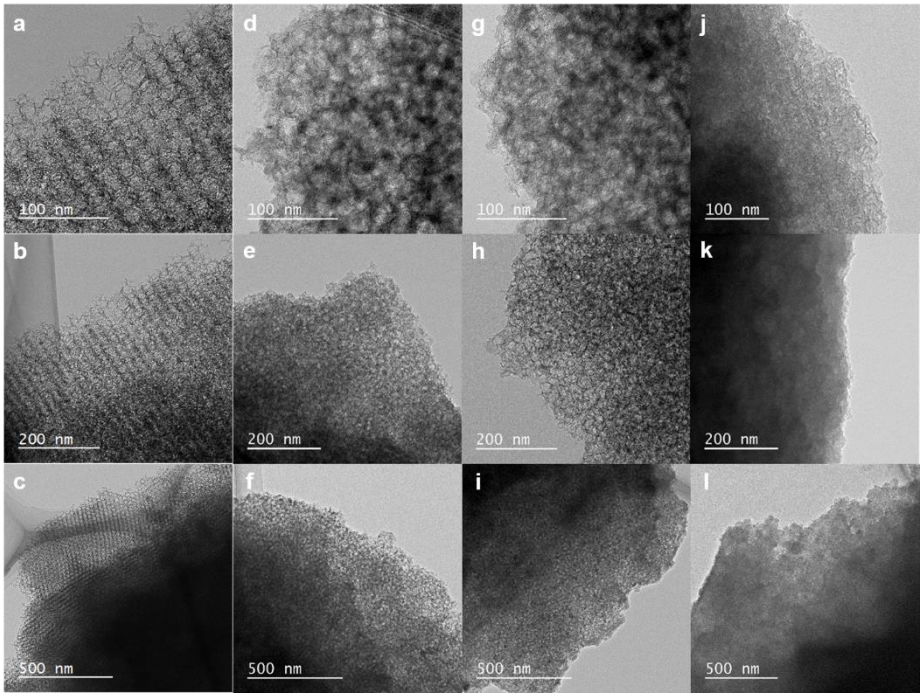

Figure 3.8. TEM images of (a-c) 3DOmC before cycling, and those after 1st discharge (100mA/g) for (d-f) SE, (g-i) 5VC, and (j-l) 10VC.

To further investigate the chemical components of the SEI layer, XPS analysis is done after a cycle (Fig. 3.9a and b). The O1s spectrum confirms that the polymerized VC is present in the case of 5VC [57, 59, 62, 63]. Overall, the intensity of the peaks in the higher binding energy is stronger for 5VC, indicating the presence of the oxidized byproducts of VC [59, 62, 63]. Furthermore, the F1s spectrum of 5VC shows that the peak ascribed to LiF is relatively small with respect to that of $LiPF_6$/PVdF (Fig. 3.9b). This signifies that the decomposition of $LiPF_6$ salt to LiF ($LiPF6 \rightarrow LiF + PF_5$) is largely alleviated as a result of the formation of polymerized VC [56, 59, 60]. LiF is an undesirable SEI component due to the low permeability of Li ions, and the relatively high content of LiF in the SEI layer of SE is likely responsible for the high SEI and charge transfer resistance [71-73]. On the other hand, the addition of 5 wt.% of VC mitigates the production of LiF by creating a favorable SEI layer prior to the formation of undesirable components as shown in Fig. 3.6 and 3.9b.

The cycling performances are compared, which indicates upon addition of 5 wt.% VC, the discharge capacity is markedly increased (Fig. 3.10). At the 100^{th} cycle, the discharge capacity of 5VC is 844.3 mAh g^{-1}. The increase in specific capacity is 160 mAh g^{-1}, which is equivalent to 23.4% increase over the discharge capacity of SE, 684.3 mAh g^{-1} (Fig. 3.10 a inset). The formation of a favorable SEI reduces the undesirable SEI component such as LiF, allowing easier passage

for the Li ions to reach the active material. The cycling performance is consistent with the EIS and XPS results.

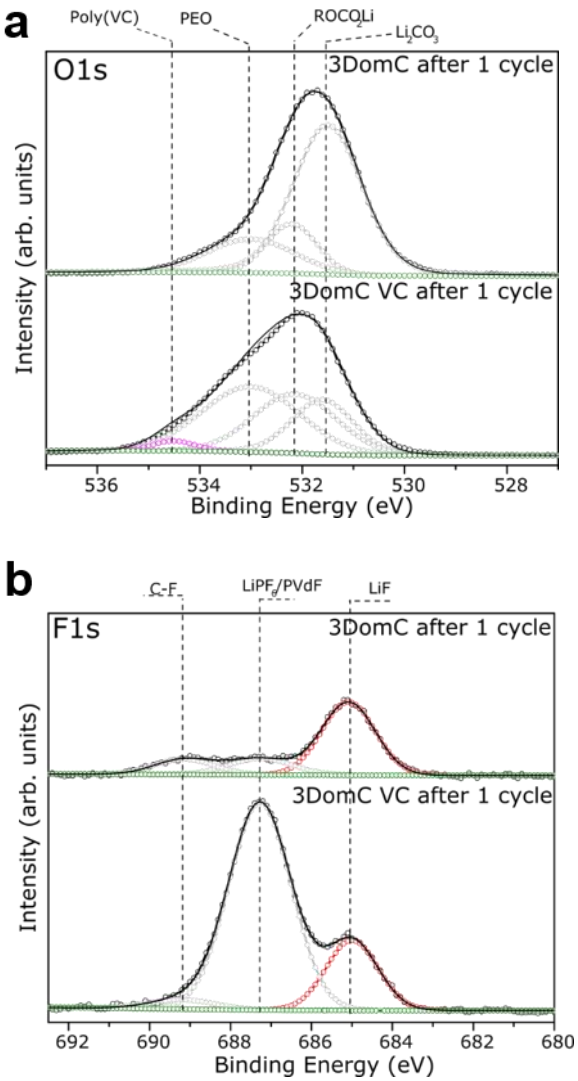

Figure 3.9. (a) O1s XPS spectra and (b) F1s XPS spectra of SE and 5VC after the 1st cycle.

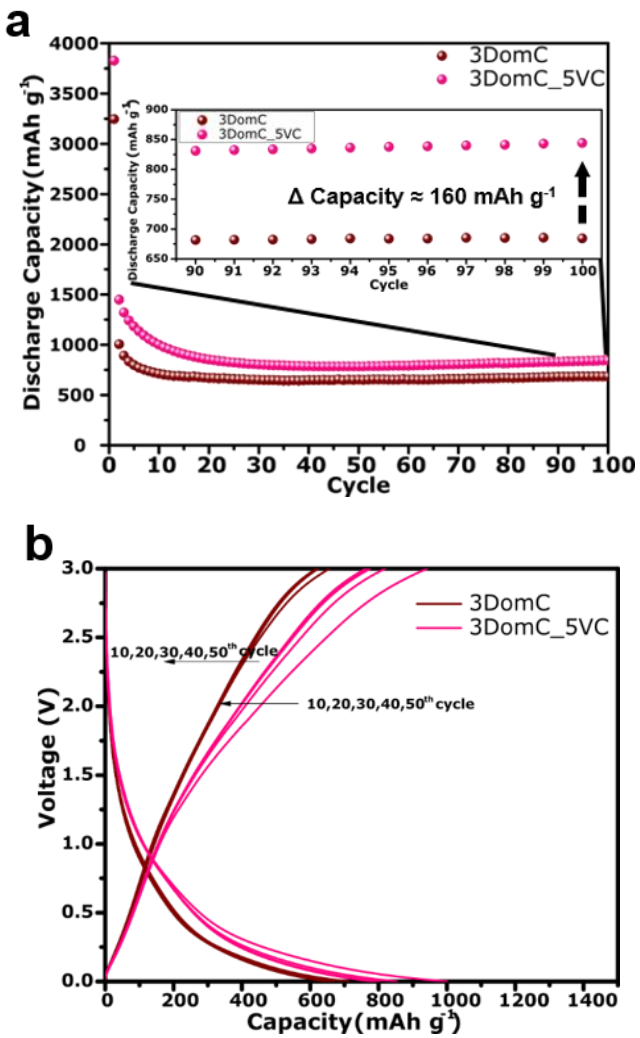

Figure 3.10. (a) Cycling performance and (b) voltage profiles of SE and 5VC.

3.4. Conclusion

We have demonstrated that the addition of 5 wt.% of VC in the electrolyte improves the discharge capacity of 3DOmC by 23.4%. The EIS and voltage profiles show that the addition of VC reduces the resistance and improves the coulombic efficiency. Furthermore, the surface analysis indicates upon addition of VC, polymerized VC forms on the electrode and the LiF content is reduced, resulting in a higher permeability of Li ions and improved performance. We believe the result shown here expands the applications of VC to improving the performance of an ordered mesoporous carbon with a high surface area, and further investigation is underway to unveil VC's effect on other non-graphitic porous carbon structures.

References

[1] J.N. Reimers, J.R. Dahn, J. Electrochem. Soc., 139 (1992) 2091-2097.

[2] P. G. Bruce, A. Robert Armstrong, R. L. Gitzendanner, J. Mater. Chem., 9 (1999) 193-198.

[3] M. Winter, J.O. Besenhard, M.E. Spahr, P. Novák, Adv. Mater., 10 (1998) 725-763.

[4] X.-Q. Yang, J. McBreen, W.-S. Yoon, M. Yoshio, H. Wang, K. Fukuda, T. Umeno, Electrochem. Commun., 4 (2002) 893-897.

[5] P. Poizot, S. Laruelle, S. Grugeon, J.-M. Tarascon, J. Electrochem. Soc., 149 (2002) A1212-A1217.

[6] H. Li, P. Balaya, J. Maier, J. Electrochem. Soc., 151 (2004) A1878-A1885.

[7] M.-K. Song, S. Park, F.M. Alamgir, J. Cho, M. Liu, Mater. Sci. Eng., R., 72 (2011) 203-252.

[8] M.S. Islam, C.A.J. Fisher, Chem. Soc. Rev., 43 (2014) 185-204.

[9] M.R. Palacin, Chem. Soc. Rev., 38 (2009) 2565-2575.

[10] A. Manthiram, Y. Fu, S.H. Chung, C. Zu, Y.S. Su, Chem. Rev., 114 (2014) 11751-11787.

[11] P.G. Bruce, S.A. Freunberger, L.J. Hardwick, J.-M. Tarascon, Nat. Mater., 11 (2012) 172-172.

[12] P.G. Bruce, B. Scrosati, J.-M. Tarascon, Angew. Chem., Int. Ed., 47 (2008) 2930-2946.

[13] H. Kim, G. Jeong, Y.-U. Kim, J.-H. Kim, C.-M. Park, H.-J. Sohn, Chem. Soc. Rev., 42 (2013) 9011-9034.

[14] Y. Li, Z.Y. Fu, B.L. Su, Adv. Funct. Mater., 22 (2012) 4634-4667.

[15] Z. Li, L. Yin, Nanoscale, 7 (2015) 9597-9606.

[16] Y. Li, H. Zhang, P. Kang Shen, Nano Energy, 13 (2015) 563-572.

[17] D.W. Wang, F. Li, M. Liu, G.Q. Lu, H.M. Cheng, Angew. Chem. Int. Ed., 47 (2008) 373-376.

[18] J. Xiao, D. Mei, X. Li, W. Xu, D. Wang, G.L. Graff, W.D. Bennett, Z. Nie, L.V. Saraf, I.A. Aksay, J. Liu, J.-G. Zhang, Nano Lett., 11 (2011) 5071-5078.

[19] N. Brun, S.R.S. Prabaharan, C. Surcin, M. Morcrette, H. Deleuze, M. Birot, O. Babot, M.-F. Achard, R. Backov, J. Phys. Chem. C, 116 (2012) 1408-1421.

[20] C.M. Doherty, R.A. Caruso, B.M. Smarsly, P. Adelhelm, C.J. Drummond, Chem. Mater., 21 (2009) 5300-5306.

[21] S. Liu, H. Jia, L. Han, J. Wang, P. Gao, D. Xu, J. Yang, S. Che, Adv. Mater., 24 (2012) 3201-3204.

[22] Z.L. Wang, D. Xu, J.J. Xu, L.L. Zhang, X.B. Zhang, Adv. Funct. Mater., 22 (2012) 3699-3705.

[23] Y.F. Yuan, X.H. Xia, J.B. Wu, J.L. Yang, Y.B. Chen, S.Y. Guo, Electrochem.

Commun., 12 (2010) 890-893.

[24] F. Zhang, K.X. Wang, G.D. Li, J.S. Chen, Electrochem. Commun., 11 (2009) 130-133.

[25] S.-X. Wang, S. Chen, Q. Wei, X. Zhang, S.Y. Wong, S. Sun, X. Li, Chem. Mater., 27 (2015) 336-342.

[26] H. Zhang, G. Cao, Z. Wang, Y. Yang, Z. Shi, Z. Gu, Nano Lett., 8 (2008) 2664-2668.

[27] J. Zhao, H. Lai, Z. Lyu, Y. Jiang, K. Xie, X. Wang, Q. Wu, L. Yang, Z. Jin, Y. Ma, J. Liu, Z. Hu, Adv. Mater., (2015) 3541-3545.

[28] C. Liang, N.J. Dudney, J.Y. Howe, Chem. Mater., 21 (2009) 4724-4730.

[29] G. He, X. Ji, L. Nazar, Energy Environ. Sci., 4 (2011) 2878-2883.

[30] C. Zhao, L. Liu, H. Zhao, A. Krall, Z. Wen, J. Chen, P. Hurley, J. Jiang, Y. Li, Nanoscale, 6 (2014) 882-888.

[31] X. Tao, X. Chen, Y. Xia, H. Huang, Y. Gan, R. Wu, F. Chen, W. zhang, J. Mater. Chem. A, 1 (2013) 3295-3301.

[32] S. Wei, H. Zhang, Y. Huang, W. Wang, Y. Xia, Z. Yu, Energy Environ. Sci., 4 (2011) 736-740.

[33] K. Xi, S. Cao, X. Peng, C. Ducati, R. Vasant Kumar, A.K. Cheetham, Chem. Commun., 49 (2013) 2192-2194.

[34] Z. Li, Y. Huang, L. Yuan, Z. Hao, Y. Huang, Carbon, 92 (2015) 41-63.

[35] Z. Li, Y. Jiang, L. Yuan, Z. Yi, C. Wu, Y. Liu, P. Strasser, Y. Huang, ACS Nano, 8 (2014) 9295-9303.

[36] S. Xin, L. Gu, N.-H. Zhao, Y.-X. Yin, L.-J. Zhou, Y.-G. Guo, L.-J. Wan, J. Am. Chem. Soc., 134 (2012) 18510-18513.

[37] Z. Li, L. Yuan, Z. Yi, Y. Sun, Y. Liu, Y. Jiang, Y. Shen, Y. Xin, Z. Zhang, Y. Huang, Adv. Energy Mater., 4 (2014) 1301473.

[38] B. Zhang, X. Qin, G.R. Li, X.P. Gao, Energy Environ. Sci., 3 (2010) 1531-1537.

[39] J. Liu, S.Z. Qiao, H. Liu, J. Chen, A. Orpe, D. Zhao, G.Q. Lu, Angew. Chem., Int. Ed., 50 (2011) 5947-5951.

[40] W.C. Yoo, N. Rajabbeigi, E.E. Mallon, M. Tsapatsis, M.A. Snyder, Microporous Mesoporous Mater., 184 (2014) 72-82.

[41] N.P. Wickramaratne, M. Jaroniec, ACS Applied Mater. Interfaces, 5 (2013) 1849-1855.

[42] K.T. Lee, X. Ji, M. Rault, L.F. Nazar, Angew. Chem., Int. Ed., 48 (2009) 5661-5665.

[43] W. Zhang, D. Qiao, J. Pan, Y. Cao, H. Yang, X. Ai, Electrochim. Acta, 87 (2013) 497-502.

[44] X. Ji, K.T. Lee, L.F. Nazar, Nat. Mater., 8 (2009) 500-506.

[45] L.F. Nazar, M. Cuisinier, Q. Pang, MRS Bull., 39 (2014) 436-442.

[46] S.S. Zhang, J. Electrochem. Soc., 159 (2012) A920-A923.

[47] A. Rosenman, R. Elazari, G. Salitra, E. Markevich, D. Aurbach, A. Garsuch, J. Electrochem. Soc., 162 (2015) A470-A473.

[48] S.S. Zhang, Electrochim. Acta, 70 (2012) 344-348.

[49] D. Aurbach, E. Pollak, R. Elazari, G. Salitra, C.S. Kelley, J. Affinito, J. Electrochem. Soc., 156 (2009) A694-A702.

[50] J. Ahn, K.J. Lee, W. Bak, J.-J. Kim, J.-K. Lee, W.C. Yoo, Y.-E. Sung, J. Phys. Chem. C, 119 (2015) 10255-10265.

[51] Y. Yang, G. Zheng, S. Misra, J. Nelson, M.F. Toney, Y. Cui, J. Am. Chem. Soc., 134 (2012) 15387-15394.

[52] Y. Wang, S. Nakamura, K. Tasaki, P.B. Balbuena, J. Am. Chem. Soc., 124 (2002) 4408-4421.

[53] S.S. Zhang, J. Power Sources, 162 (2006) 1379-1394.

[54] J.-J. Kim, T. Yoon, K.J. Lee, S.-H. Yu, S.M. Oh, Y.-E. Sung, J. Nanosci. Nanotechnol., 13 (2013) 7924-7931.

[55] D. Xiong, J.C. Burns, A.J. Smith, N. Sinha, J.R. Dahn, J. Electrochem. Soc., 158 (2011) A1431-A1435.

[56] D. Aurbach, K. Gamolsky, B. Markovsky, Y. Gofer, M. Schmidt, U. Heider, Electrochim. Acta, 47 (2002) 1423-1439.

[57] G. Zampardi, F. La Mantia, W. Schuhmann, Electrochem. Commun., 58

(2015) 1-5.

[58] S.-K. Jeong, M. Inaba, R. Mogi, Y. Iriyama, T. Abe, Z. Ogumi, Langmuir, 17 (2001) 8281-8286.

[59] H. Ota, Y. Sakata, A. Inoue, S. Yamaguchi, J. Electrochem. Soc., 151 (2004) A1659-A1669.

[60] M. Herstedt, H. Rensmo, H. Siegbahn, K. Edström, Electrochim. Acta, 49 (2004) 2351-2359.

[61] D. Takamatsu, Y. Orikasa, S. Mori, T. Nakatsutsumi, K. Yamamoto, Y. Koyama, T. Minato, T. Hirano, H. Tanida, H. Arai, Y. Uchimoto, Z. Ogumi, J. Phys. Chem. C, 119 (2015) 9791-9797.

[62] L. El Ouatani, R. Dedryvère, C. Siret, P. Biensan, D. Gonbeau, J. Electrochem. Soc., 156 (2009) A468-A477.

[63] L. El Ouatani, R. Dedryvère, C. Siret, P. Biensan, S. Reynaud, P. Iratçabal, D. Gonbeau, J. Electrochem. Soc., 156 (2009) A103-A113.

[64] M. Itagaki, S. Yotsuda, N. Kobari, K. Watanabe, S. Kinoshita, M. Ue, Electrochim. Acta, 51 (2006) 1629-1635.

[65] O. Matsuoka, A. Hiwara, T. Omi, M. Toriida, T. Hayashi, C. Tanaka, Y. Saito, T. Ishida, H. Tan, S.S. Ono, S. Yamamoto, J. Power Sources, 108 (2002) 128-138.

[66] H. Fujimoto, A. Mabuchi, K. Tokumitsu, T. Kasuh, J. Power Sources, 54 (1995) 440-443.

[67] T. Zheng, Y. Liu, E.W. Fuller, S. Tseng, U. von Sacken, J.R. Dahn, J.

Electrochem. Soc., 142 (1995) 2581-2590.

[68] W. Fan, M.A. Snyder, S. Kumar, P.-S. Lee, W.C. Yoo, A.V. McCormick, R. Lee Penn, A. Stein, M. Tsapatsis, Nat. Mater., 7 (2008) 984-991.

[69] B. Han, E.J. Lee, W.H. Choi, W.C. Yoo, J.H. Bang, New J. Chem., 39 (2015) 6178-6185.

[70] M. Itagaki, N. Kobari, S. Yotsuda, K. Watanabe, S. Kinoshita, M. Ue, J. Power Sources, 135 (2004) 255-261.

[71] D. Aurbach, K. Gamolsky, B. Markovsky, G. Salitra, Y. Gofer, U. Heider, R. Oesten, M. Schmidt, J. Electrochem. Soc., 147 (2000) 1322-1331.

[72] D. Aurbach, B. Markovsky, A. Shechter, Y. Ein-Eli, H. Cohen, J. Electrochem. Soc., 143 (1996) 3809-3820.

[73] Y. Fan, J. Wang, Z. Tang, W. He, J. Zhang, Electrochim. Acta, 52 (2007) 3870-3875.

국문초록

리튬-이온 및 리튬-황 전지에서의 다공성 탄소물질의 전기화학적 특성

첨단 전지산업의 시대가 도래함에 따라 휴대용 전자기기뿐만 아니라 전기자동차용 이차전지의 수요가 기하급수적으로 늘어나고 있다. 이에 소비자들이 필요로 하는 이차전지의 성능향상 또한 기하급수적으로 증가하고 있는 추세이다. 이때까지 주로 소형 정보기술 기기의 에너지원으로 사용돼오던 에너지 저장 및 변환 장치들의 용도가 더욱 넓어짐에 따라 기술력의 향상 또한 요구되고 있다. 특히, 리튬이온전지에서는 에너지 밀도나 출력특성 향상을 위해 많은 연구가 진행되고 있다. 그럼에도 불구하고 전기차 전력 원으로서는 아직까지는 용량, 고속 충방전, 및 장기성능 등이 부족한 실정이다.

특히 양극 물질 경우 새로운 후보물질 개발이 절실하다. 주로 사용되는 활물질인 리튬코발트산화물 ($LiCoO_2$) 경우 코발트 (Co) 의 독성 및 높은 수요 때문에 가격 경쟁력을 점점 잃고 있는 물질이다. 이를 대체할 만한 고용량 양극물질로 망가니즈 계열의 Overlithiated Layered Oxide (OLO), 타보라이트 (tavorite), 규산염 (silicate), 및 붕산염 (borate) 등이 연구가 되고 있지만 물질들의 용량들이 기존의 물질들에 비해 획기적으로 차이가 나지 않아 차세대 에너지 저장물질로 적합한지 의문이 든다.

이와 같은 점들을 고려하여 가격적으로 확실히 경쟁력이 있는 황을 활물질로 사용하는 리튬-황 전지가 제시되었다. 하지만 이 시스템 경우 활물질

이 전해질로 용해되고, 전도도가 낮아 속도적으로 제한이 있으며, 충방전시 부피팽창이 80%정도 일어나 개선되어야 할 점들이 많다. 이를 보완하기 위해 여러 연구들에서는 기공구조가 발달되어 있는 나노 탄소 입자들에 황을 넣은 활물질을 사용하여 리튬-황 배터리에 적용하였다.

첫 번째 연구에서는 마이크로/메조 기공구조가 발달되어 있는 나노탄소 입자들을 리튬-황 배터리에 적용하여 이와 관련된 전기화학 반응들을 다양한 방법으로 분석을 하였다. 리튬–황 배터리에서는 활물질이 갖는 2 nm 이하의 마이크로 기공들이 황이 녹아 나가는 것을 막고 2~50 nm 사이의 메조 기공들이 전해질의 물질이동을 향상시켜 장기성능을 개선했다는 설명들이 많지만, 각 기공들이 전기화학 반응에 어떤 영향을 미치는지 직접적으로 확인한 자료들이 없다. 각 기공들의 영향을 확인하기 위해 마이크로/메조 기공구조가 조절된 모델 시스템을 고안하였고, 이를 레조르시놀-포름알데히드 고분자 (resorcinol-formaldehyde polymer) 구형들을 탄소화 시킨 이후 이산화탄소로 활성화 시키는 방법을 이용하여 구현하였다. 탄소의 마이크로/메조 기공구조는 탄소화된 나노입자들을 이산화탄소로 활성화하는 시간을 바꿔 조절하였고, 질소 흡착실험을 통해 1.2 nm 이하의 기공들이 발달된 작은 마이크로 기공 탄소 (small micropore carbon)와 마이크로 및 메조 기공들이 발달된 계층형 마이크로 기공 탄소 (hierarchical microporous carbon)가 만들어졌음을 확인하였으며, 마이크로/메조 기공구조에 따른 탄소의 구조 및 물성과 흡착된 황의 물성을 라만 (Raman), X선 회절 분석 (XRD) 및 투과전자현미경 (TEM)으로 확인하였다. 그리고 작은 마이크로 기공 탄소와

계층형 마이크로 기공 탄소 각각에 황을 흡착시킨 샘플들의 전기화학 반응을 비교하여 계층형 기공 탄소/황 합성물의 경우 충방전 시 마이크로 기공에 들어있는 황이 사이클이 지남에 따라 서서히 가역적으로 활성화됨을 충방전 프로파일, dQ/dV plot, galvanostat intermittent titration technique (GITT) 그리고 X선 광전자 분광법 (XPS)를 통해 확인하였다. 또한 1.8 V 이하에서 질산리튬 ($LiNO_3$)의 부반응으로 형성되는 물질들이 활성화 되는 반응에 어떠한 영향을 끼치는지 연구해 보았다. 이러한 현상을 실리카로 만든 단단한 템플릿 (silica hard template)을 사용하여 페놀-포름알데히드 (phenol-formaldehyde)로 만든 메조 기공구조 탄소물질로 재확인하였고, 이러한 현상이 생기는 메커니즘에 대해서 규명을 하였으며, 이를 통해 리튬-황 배터리 활물질의 최적 기공구조를 제안하였다.

두 번째 연구에서는 메조 기공구조, 특히 물질이동이 용이한 3 dimensional-ordered mesoporous carbon (3DOmC)을 리튬이온배터리에 적용하였다. 리튬이온배터리 문제점들 중 하나인 낮은 용량의 경우, 물질들이 이론적으로 함유할 수 있는 리튬의 양이 제한적 이기 때문에 활물질의 선택이 중요하다. 이에 실리콘 (Si), 저마늄 (Ge), 금속산화물 (Metal oxide), 칼코게나이드 (chalcogenide) 등 고용량 음극소제들에 대한 연구가 많이들 진행되고 있다. 하지만 대체로 많은 양의 리튬이온들을 함유할 수 있는 물질들 경우 부피팽창에 의한 성능저하가 과속화되면서 안정적인 성능을 발현하기가 어려운 물질들이다. 이에 비해 기공구조가 잘 발달되어 있는 탄소 경우, 상대적으로 부피팽창이 적으나 고용량을 발현할 수 있다는 점에서 장점이 있다. 하지만 높은 표면적 때문에 표면처리를 통한 리튬이온전지의 부차적인 반응을 최소화시키는 연구가 필요하다. 이는 우리가 원하는 전

기화학적 반응 또한 표면에서 일어나는 반응이기 때문이다. 리튬이온들과 활물질들이 효율적으로 반응하려면 전극표면에 생기는 피막을 최적화할 필요가 있다.

이에 두 번째 연구에서는 적절한 농도의 비닐렌카보네이트 (VC)를 첨가하여 양질의 피막을 만들었고 이를 통해 낮은 쿨롱효율 및 용량을 개선하였다. 이 때, X 선 광전자 분광법 와 교류 임피던스 분석법 (EIS)를 이용하여 비닐렌카보네이트 (VC)가 첨가되었을 때 생성된 solid electrolyte interface (SEI) 피막은 일반적인 SEI 에 비해 리튬이온 저항이 큰 불화리튬 (LiF) 함량이 낮음을 확인하였다. 이를 통해 3DOmC 의 넓은 비표면적이 갖는 한계를 보완하며 동시에 물질이동의 이점을 살릴 수 있는 리튬이온배터리를 만들 수 있었다.

이 연구들을 통해 리튬-황 배터리 관련 연구 경우 기공구조 안에서 일어나는 반응 메커니즘에 대해서 새로이 분석하였고, 물질에 적용되는 전류 및 반응전위 범위에 따라서 활성화 될 수 있는 황의 용량에 큰 차이가 있다는 것을 발견을 하였다. 이는 기존에 알려진 전류 및 반응전위에서 활성화가 없었기에 실제 사용된 황이 생각보다 적음을 알 수 있다는 점에서 의미를 가질 수 있다. 리튬-이온 배터리 관련 연구 경우, 기존에 연구해왔던 실리콘, 금속산화물, 및 칼코게나이드 외에 높은 표면적을 갖고 있는 탄소물질 또한 적합하다는 것을 알 수가 있다. 성능을 더욱더 개선시키려면 표면에 생기는 피막의 성분을 개선 시킴으로써 더 나은 용량을 얻을 수 있다는 점에서 의미를 갖는다.

주요어: 전기화학, 표면분석, 리튬 이온 전지, 리튬 황 전지, 기공탄소

학 번: 2012-31299